# Polarimetric SAR Interferomerty based Inversion Modelling for Tree Height Estimation

**GAUTAM SOLANKI**

**March, 2016**

**IIRS Supervisor:**

Shashi Kumar

**ITC Supervisor:**

Dr. Valentyn Tolpekin

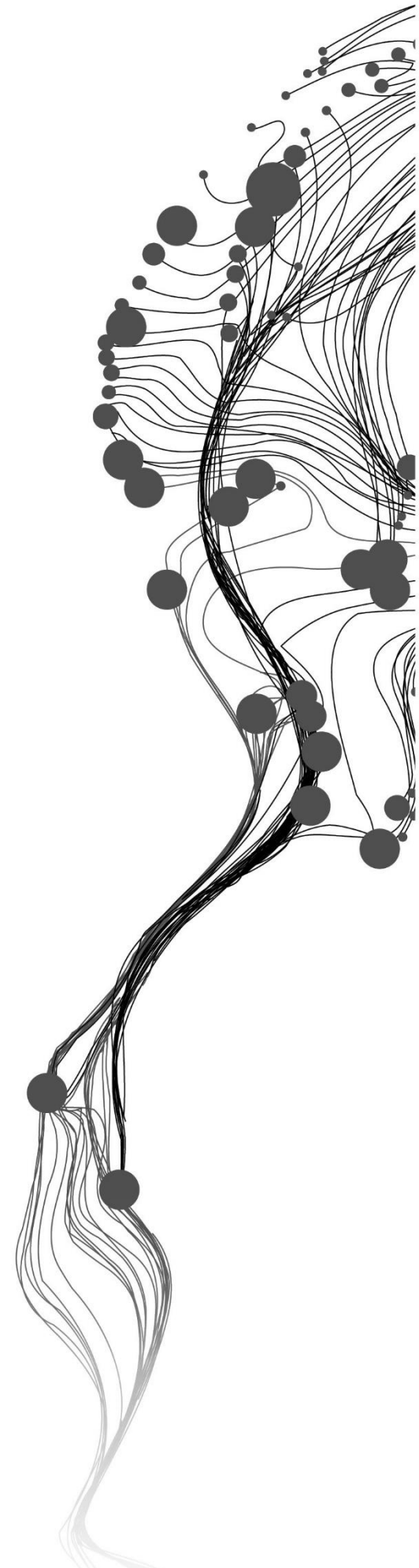

# Polarimetric SAR Interferomerty based Inversion Modelling for Tree Height Estimation

GAUTAM SOLANKI

Enschede, The Netherlands, March, 2016

Thesis submitted to the Faculty of Geo-Information Science and Earth Observation of the University of Twente in partial fulfilment of the requirements for the degree of Master of Science in Geo-information Science and Earth Observation.

**Specialization**: Geo-informatics

## SUPERVISORS:

| | |
|---|---|
| IIRS Supervisor | : Mr. Shashi Kumar, IIRS |
| ITC Supervisor | : Dr. Valentyn Tolpekin, ITC |

## THESIS ASSESSMENT BOARD:

| | |
|---|---|
| Chair | : Dr. A.A. Voinov |
| ITC Professor | : Prof. Dr. Ir. A. Stein |
| External Examiner | : Dr. Anup Kumar Das (SAC, Ahmadabad) |

## OBSERVERS:

| | |
|---|---|
| IIRS Observer | : Dr. S.K Srivastav, Dr. Sameer Saran |
| ITC Observer | : Dr. Valentyn Tolpekin, Dr. N.A.S. Hamm |

## DISCLAIMER

This document describes work undertaken as part of a programme of study at the Faculty of Geo-Information Science and Earth Observation of the University of Twente. All views and opinions expressed therein remain the sole responsibility of the author, and do not necessarily represent those of the Faculty.

*Dedicated to my Parents……*

# ABSTRACT

This study describes the effect of shift in polarization orientation angle on PolInSAR data for the estimation of tree height in forested areas. Polarization orientation angle (POA) shift has been researched on Polarimetric SAR (PolSAR) data leading to its effects on coherency matrices. The analysis of POA on coherence of PolInSAR data to estimate forest tree height, is a novel study presented in this thesis. Barkot and Thano range was selected as the study area falling in the Dehradun district of Uttrakhand state in India. The most dominant species found is the *Shorea Robusta* (Sal) with maximum height of 29 m. For the validation and accuracy assessment, ground truth were taken in both the ranges. 90 samples plots were selected and the average of tree heights in each plot were measured. The effect of POA is demonstrated on the PolInSAR pair of 2013 and 2014. Baseline was small in both the dataset so it was simulated to obtain the optimal baseline for forest tree height retrieval.

Coherence Amplitude Inversion modelling technique was utilized for the forest tree height estimation. The accuracy of the forest tree height is assessed using *in-situ* measurements. The overestimation of tree height in non-forested areas is also addressed through this thesis. Coherence was calculated in all possible polarization combinations. Coherence changes are observed from 2013 to 2014 due to the lower incidence angle in 2014 dataset. This leads to the overestimation of tree height in 2014 dataset. The coherence after POA shift shows decrease in double bounce scattering and random change in volume scattering. The average accuracy of tree height decreased from 88.88 % to 88.49 % for 2013 and 85.59 % to 84.32 % in 2014. The accuracies suggested that it is possible to obtain forest tree height using PolInSAR coherence. The small change in accuracies and no significant change in coherence suggested that POA compensation is not required on PolInSAR dataset.

**Keywords:** Coherence Amplitude Inversion modelling Technique (CAI), Coherence, Polarimetric SAR interferometry, Tree height, Baseline.

# ACKNOWLEDGEMENTS

This thesis arose as a part of M.Sc. project work carried out at Indian Institute of Remote Sensing and ITC, The Netherlands. This thesis would not have been materialized without the proper guidance and support of many people. This is a humble acknowledgement to convey my gratitude to all of them. I would like to express my deepest gratitude to my IIRS supervisor MR. Shashi Kumar for giving me opportunity to work in this project. Without his valuable guidance, support and motivation this research work would not have been possible. He gave me the freedom to learn from my mistakes. His patience and support cannot be valued.

I am thankful to my ITC supervisor for trusting my capabilities and encouraging me with his great wisdom. Without his regular feedback and direction, the completion of this work would not have been easy going.

I would like to express my sincere gratitude to our IIRS Director Dr. A. Senthil Kumar for providing all the opportunities and facilities. My sincere thanks to former course coordinator Dr. S. K. Srivastav, Group Head, IIRS and Dr. N. Hamm, Asst. Professor, ITC, and present course coordinator Dr. Sameer Saran, HOD, GID, IIRS for their continuous concern and encouragement.

I would like to thank my lovely parents for being there in my life for their love and support in all up and downs.

I would like to say thank to my IIRS friends Anchit, Ajit, Rajan, Aparna, Amit, Sayan, Nitin, Shrija Arnab, Nikita, Sanjay for all the masti time we had together.

I am especially thankful to my friend Anshul Rohilla and Beenu Virmani for continuous support and faith in me.

I would also like to say thanks to my friends at ITC Ipsit Das, Honore, Melkom, Maral, Yalda, John, Erika for making my stay memorable at ITC.

Lastly, I offer my regards to all those who knowingly and unknowingly have supported me during the completion of this project work.

# TABLE OF CONTENTS

# LIST OF FIGURES

# LIST OF TABLES

# 1. INTRODUCTION

Forest plays a very important role for the survival of living beings on the planet Earth. According to the report of the Food and Agriculture Organization (2010), the forest covered around 31 % of the land surface of the Earth which was approximately four billion ha in 2010. An expected 13 million ha of woodlands were lost every year somewhere from 2000 and 2010 because of deforestation. In tropical rain forests, especially, deforestation keeps on being an earnest ecological issue that heightens a dangerous atmospheric deviation. Forests affect our day to day lives significantly which we can envision. Simply consider how woods have influenced your life today: Have you had your breakfast? Perused a daily paper? Set out to work in transport? Made a shopping, rundown? These exercises are directly or indirectly associated with the use of timber. The rapid demands of the population increase the consumption of natural resources. In recent years, about a large portion of the world's unique timberland spread has been lost due to the unsystematic utilization of its assets. When we take away the woods, it is not only the trees that go, the whole biological system starts to go into disrepair with adverse impact on every one of us. Forest and atmosphere are naturally connected, forest loss, and debasement is both causing an impact on our evolving atmosphere. Change in temperature due to the increase of carbon dioxide in the atmosphere is affecting our ecosystem. Forests absorb approximately one-third of recent anthropogenic emission of carbon dioxide to the atmosphere (Percy et al., 2005), the research in biomass estimation addresses these issues. Biomass has been considered an imperative parameter to quantify the adjustments in forest structure (Husch et al., 2002). For accurate estimation of biomass, the appropriate extraction of tree parameters such as tree height, the volume of the tree, diameter at breast height is essential. Optical remote sensing information has been used previously in segregating forest type, density, and extent. The optical sensor are used to recognize forest canopy. However, the constraint with them was that they could not identify the forest structure. Now a days, remote sensing using high spatiotemporal resolution plays a critical part in forest monitoring. The remote sensing technique is preferable in the monitoring of areas that are distant for field observations. There are many remote sensing techniques that are being used to estimate the biomass by retrieving the tree parameters. Several studies have been carried out to obtain the forest height such as in studies were done by Mette et al. (2004) and Caicoya et al. (2015).

## 1.1 RADAR Remote Sensing

The introduction of RADAR remote sensing is essentially required to monitor the vast area of forest. In general, RADAR with longer antenna and narrower beam width have the ability to achieve high spatial

resolution from space borne platforms. This ability leads to the improved detection of the objects under observation. Implementation of long satellite antenna for high image resolution is impractical; therefore, Synthetic Aperture Radar (SAR), which uses signal processing technique to improve the resolution has been introduced as a viable alternative. SAR uses the technique of virtual aperture that is much longer than the physical antenna length to increase the resolution of the radar image. For forest mapping and monitoring along with other remote sensing applications, SAR system uses wavelengths which are categorized according to the frequency. The opreating feequencies of SAR include X-band (uses frequency ranges from 12.5 to 8 GHz) in which penetration is minor and is dominated by leaf interactions while C-band (uses frequency from 8 to 4 GHz) can penetrate deep into the canopy and dominated by twigs, small branches (Solberg et al., 2003). L-band (uses frequency from 1 to 3 GHz), P-band (uses 0.99 to 0.29 GHz) can penetrate deep into the canopy and contribute surface, double bounce (ground-tree interaction) and volume scattering from the canopy (Wang et al., 1994). Polarimetric Synthetic Aperture Radar (POLSAR) is used to extract scattering information in determining various physical properties such as shape, orientation and dielectric properties of the target, but as a limitation, the data image acquisition is as complicated as calibration and validation and also lacks information about depth (Boerner et al., 2003). Similarly, Interferometric SAR (INSAR) informs about the scatter's information in the vertical plane and also provides the digital elevation model maps, but lacks the ability to discriminate the origin of backscattering returns from which interferograms are constructed (Balmer & Hartl, 2000). Polarimetric Interferometric Synthetic Aperture Radar (POLINSAR) is not only sensitive to the distribution and shape of vegetation scatters in POLSAR but is also sensitive to the spatial distribution of vegetation height in INSAR. Hence, it is more advantageous than both POLSAR and INSAR alone in extracting information of vertical vegetation structure (Hongjun et al., 2007). In view of the above argumentation, usage of POLINSAR in forest inventory mapping could be a viable research focus.

## 1.2 Problem Statement

This project will focus on retrieving the height information of the tree and as a pre-requisite estimation of the Polarization Orientation Angle (POA) will be done. POA is the angle subtended by the semi-major axis of the polarization ellipse with the horizontal axis. Synthetic aperture radar acquisition of horizontal surface gives horizontal polarization electric field parallel to the surface, but for tilted surface it is no longer parallel to the surface. As a result, horizontal transmitting and receiving radar response gets affected. Similarly, vertical transmitting and receiving radar responses will also get affected (Lee et al., 2000). It is the characteristics of the electromagnetic wave which gets influenced by the scattering from haphazard forest structures and surface undulation (Woodhouse, 2005). Iribe & Sato (2007) have carried out the work to show the effect of the shift in POA of PolSAR dataset. It was literature evidence suggests

that there was always overestimation in volume scattering and underestimation in double-bounce scattering particularly in the forested area (Lee & Ainsworth, 2009). Moreover, it was found that by decreasing the frequency, the shift in POA increases. Methodologies have been developed by researchers to compensate the shift in POA in the PolSAR dataset (Iribe & Sato, 2007). Among several approaches, one approach used was compensation of the dataset from POA in coherency matrix and implementation of the same on scattering matrix (Lee & Ainsworth, 2009). In previous studies, there has been a research gap to implement the concept of POA compensation on POLINSAR data, and this is a very important factor which may affect the acquisition. This study will investigate the effect of POA on POLINSAR data and adopt a technique to compensate the dataset for doing POLINSAR based modeling for retrieving forest tree height.

## 1.3 Research Identification

### 1.3.1 Research Objective

The prime focus of the study is to retrieve the forest tree height using POLINSAR inversion modeling and to evaluate the effect of POA compensation on POLINSAR data.

### 1.3.2 Sub-Objectives

- To study the Polarization Orientation Angle shift on POLINSAR data.
- To study the coherence contributed by forest area.
- To estimate the forest height before and after POA compensation.
- To validate and to assess the accuracy of estimated tree height.

### 1.3.3 Research Questions

- What is the effect of POA shift on POLINSAR data?
- How coherence changes after POA compensation?
- What will be the effect of POA shift on tree height?
- What will be the accuracy obtained before and after POA shift for tree height?

## 1.4 Innovation aimed at

Previous studies suggested that effect of POA on PolSAR data plays an important role in the estimation of different scattering elements. But, results of PolSAR data showed over estimation of volume scattering and underestimation of double-bounce scattering. This anomaly was taken care of with the help of de-orientation process which includes the compensation of polarization orientation angle. Therefore, the

prime focus of this study is to see the effect of POA compensation on coherence for PolInSAR dataset, as it plays an important role in the retrieval of forest tree height.

## 1.5 Synopsis:

This thesis comprises of the following five chapters:

Chapter 1 presents the overview of how forest is important for the survival of mankind on the planet earth and also the importance of estimating biomass to address these issues. It also presents the technologies involved in active radar remote sensing for estimating biomass. This chapter throws light on the problem statement, innovation, objectives and research questions.

Chapter 2 presents the overview of basics of electromagnetics and Polarization ellipse. The research in polarization orientation angle shift, POLSAR and INSAR are reviewed. For tree height estimation, the use of SAR with the combination of POLSAR and INSAR to form POLINSAR and LIDAR are explained in this chapter.

Chapter 3 This chapter gives a brief elucidation about the study area, the dataset with equipment, and software used. It also explains the methods of field surveys for the accuracy assessment of results.

Chapter 4 includes the research approach or methods to achieve the goals of the study. The main part of this chapter includes the method used for the orientation angle estimation and the study of orientation angle shift on POLINSAR data. The model used for modeling of the tree for height estimation is also included in this chapter. The study of vertical wave number and baseline simulation along with the technique used for tree height estimation are explained.

Chapter 5 summarizes the research results of the change in coherence and tree height. The validation using field data and accuracy assessment are also incorporated in this chapter.

Chapter 6 provides the conclusions made from the present study.

# 2. Literature Review

## 2.1 Synthetic aperture radar polarimetry (POLSAR)

Polarization is one of the important properties of the electromagnetic wave that influence the transmission characteristics of SAR systems. SAR polarimetry derives qualitative and quantitative physical information on snow, land, ice, ocean and urban applications based on the polarimetric properties of natural and man-made scatters (Moreira et al., 2013). This capability of POLSAR is beneficial in detection and categorization of objects. When a radar wave strikes the target, it changes the polarization of the transmitted wave. It means that the transmitted and received waves differ in polarization. A complex SAR system is designed in such a way that it can transmit and receive different polarization such as horizontal (H) and vertical (V) polarization. A system with both horizontal and vertical polarizations have four polarimetric channels such as HH, VV, HV, VH, where HH means that a horizontally transmitted wave is transmitted and received. Similarly, for VV it means that a vertical wave is transmitted and received and for VH a vertical wave is transmitted, and the horizontal wave is received and so on. The HV and VH are called cross-polarized waves whereas HH and VV are called co-polarized waves. The single polarized system is defined as the system which transmits and receive either HH or VV polarized wave. Similarly, Dual Polarized system consists of HH and VV or HH and HV or VV and VH and at last, the quad-polarization system can transmit and receive all combinations of polarizations (Massonnet & Claude, 2008). The 2x2 complex scattering matrix contains the information from these channels. This 2x2 complex scattering matrix of SAR polarimetry describes the backscatter information of the target for all the polarizations and establish the relationship between the transmitted and scattered electromagnetic wave from a resolution cell (Jin & Xu, 2013).

$$[S] = \begin{bmatrix} S_{HH} & S_{HV} \\ S_{VH} & S_{VV} \end{bmatrix} \qquad (2.1)$$

The scattering matrix in equation (2.1) is obtained for each pixel of SAR image and measure the amplitude and phase of each element in complex number. The diagonal elements of scattering matrix are called co-polarized and off-diagonal elements are called cross-polarized channels. There are two configurations of the radar system, i.e. monostatic and bistatic system. The monostatic system assumes reciprocity i.e. $S_{HV}=S_{VH}$ and carries the same information in the cross-polarized channel. Scattering matrix is analyzed only in the case of pure targets. By using a scattering matrix, it is not possible to extract all the information about different types of scatters from the single pixel so, we decompose the scattering matrix by using coherency or covariance matrices. The 3×3 coherency matrix [T] extracts the polarimetric parameters for

complex targets (Touzi et al., 2004). This 3×3 coherency matrix can be described by nine parameters whose decomposition results in the physical information of the target (Pottier & Lee, 2009):

$$\begin{bmatrix} < |S_{HH} + S_{VV}|^2 > & < (S_{HH} + S_{VV})(S_{HH} - S_{VV})^* > & 2 < (S_{HH} + S_{VV}){S_{HV}}^* > \\ < (S_{HH} - S_{VV})(S_{HH} + S_{VV})^* > & < |S_{HH} - S_{VV}|^2 > & 2 < (S_{HH} - S_{VV}){S_{HV}}^* > \\ 2 < S_{HV}(S_{HH} + S_{VV})^* > & 2 < S_{HV}(S_{HH} - S_{VV})^* > & 4 < |S_{HV}|^2 > \end{bmatrix} \quad (2.2)$$

where

<...> assuming homogeneity of the random medium, it indicates spatial ensemble averaging.

The decomposition process of the coherency matrix provides an interpretation based on physical constraints i.e. how the target behave to the changes in wave polarization basis (Lee & Pottier, 2009). A model based incoherent decomposition technique by Freeman & Durden (1998) decomposes the target into three scattering mechanisms- surface scattering, double-bounce scattering, and volume scattering. This technique fails in the case of complex features, and then Yamaguchi et al. (2005) introduced the helix scattering as a fourth scattering mechanism. Usually, this fourth scattering mechanism is more prominent in urban areas, but less prominent in natural features (Yamaguchi et al., 2005). During the decomposition process of the coherency matrix, the analysis of surface, double-bounce and volume scattering for a pixel or group of pixel takes place (Cloude & Pottier, 1996).

## 2.2 Polarization ellipse

When electric field traces out a geometrical structure in a three-dimensional space and time, it follows a helical trajectory along the z-axis. Let $t_0$ is the time taken by the wave to complete one cycle, then it describes a characteristic elliptical locus of the field called as polarization ellipse. Figure 2.1 gives graphical representation of polarization ellipse (Cloude, 2010).

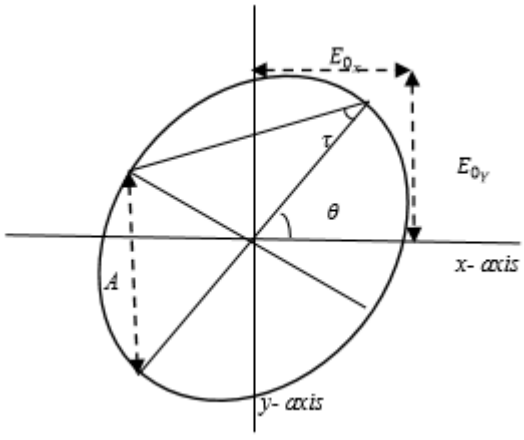


Figure 2.1 Graphical Representation of the Polarization Ellipse. 'A' is the amplitude of the ellipse, θ is the orientation angle, τ is the ellipse aperture.

The three parameters as shown in figure 2.1 can be described as (Pottier & Lee, 2009):

A is the amplitude of the ellipse and determined from the ellipse axis as:

$$A = \sqrt{E_{0_x}^2 + E_{0_y}^2} \qquad (2.3)$$

$\theta$ is the orientation angle of the ellipse and is defined as the angle between the semi-major axis and the horizontal axis.

$$\tan 2\theta = 2\frac{E_{0_x}E_{0_y}}{E_{0_x}^2 - E_{0_y}^2}\cos\delta \quad with \quad \delta = \delta_y - \delta_x \qquad (2.4)$$

Ellipticity is defined as:

$$|\sin 2\tau| = 2\frac{E_{0_x}E_{0_y}}{E_{0_x}^2 + E_{0_y}^2}|\sin\delta| \qquad (2.5)$$

where $\delta$ represents the phase difference between the horizontal and vertical component of electric field.

## 2.3 Polarization orientation angle shift

When SAR images a rugged terrain area, the polarization state of microwave gets affected, i.e. horizontal polarization electric field is parallel to the horizontal surface, but for tilted image this horizontal vector is no longer parallel to the surface. As a result, horizontally-transmitting and horizontal receiving responses from the radar are affected by the tilted slope. In the same way vertically transmitted and vertically received responses are also affected by tilted slope (Lee et al., 2000). The ellipticity angle of the polarization ellipse and the polarization orientation angle are characterized by the polarization state of the microwave. The polarization Orientation Angle (POA) is defined as an angle between the major axis of the polarization ellipse and the horizontal axis (Iribe & Sato, 2007).

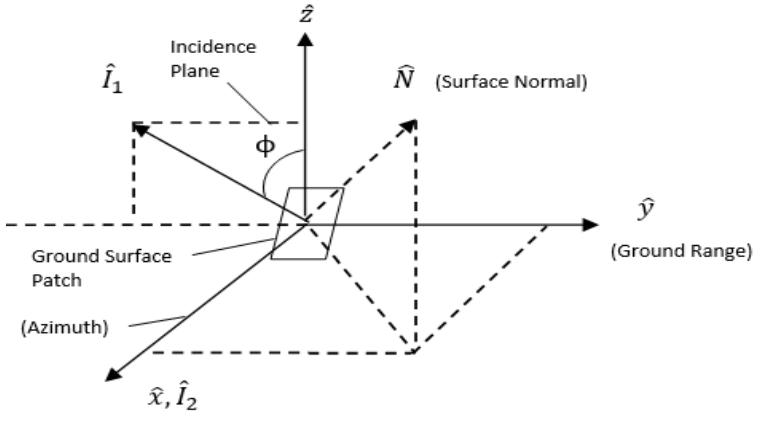


Figure 2.2 Diagram relates the orientation angle to the ground slope

where

$(\hat{x}, \hat{y})$ defines horizontal plane.

$(\hat{y}, \hat{z})$ defines radar incidence plane.

The reverse direction of axis $\hat{I}$, defines the radar line of sight.

The $\hat{x}$ axis is the direction in which satellite is moving.

$\hat{y}$ axis is in the ground range direction

$\hat{N}$ is the surface normal

For a tilted surface, surface normal is no longer in the incidence plane . Hence, there is a shift of angle θ that rotates the incidence plane$(\hat{y}, \hat{z})$. The induced shift in POA due to azimuth and range is given by (Lee & Ainsworth, 2011).

$$\tan\theta = \frac{\tan\omega}{-\tan\gamma\ \cos\varphi + \sin\varphi} \qquad (2.6)$$

where

$\theta$ is orientation angle shift.

$\tan\omega$ is azimuth slope.

$\tan\gamma$ is a slope in the ground range direction.

$\varphi$ is radar look angle.

The element of scattering matrix is affected by the induced shift in polarization orientation angle (Lee & Ainsworth, 2011) which leads to the inaccurate information extraction from the coherence or covariance matrix. As a result the double-bounce scattering power decreases and volume scattering power increases. There are two approaches for the estimation of Polarization Orientation Angle ( Lee et al., 2000):

- DEM approach
- Estimation using POLSAR data

The digital elevation model (DEM) from SAR interferometry computes azimuth and range slopes to obtain orientation angle from equation **(**2.6**).** The image so obtained is a gray scale image, scaled between $\pm 45°$ i.e. black represents -45° and white represents 45°. The obtained orientation angle can be used to correct azimuth slope effect. The disadvantage with DEM approach is the non-availability of the DEM, but orientation angle can be derived from POLSAR data without using the DEM. There are many methods to compute the orientation angle using POLSAR data (Lee et al., 2000):

- Based on peak-shift in co-polarization
- Based on circular polarization

- In-coherent polarimetric target decomposition
- Eigenvector-based decomposition
- N- target decomposition

Lee et al. (2000) found that circular polarization method is slightly better than the polarization signature method and much better than the target decomposition method. So circular polarization method is selected for the estimation of orientation angle. Further, this calculated orientation angle is used for compensating the azimuth slopes effects.

## 2.4 Interferometry synthetic aperture radar (INSAR)

SAR interferometry is a remote sensing technique that uses a high-resolution pair of SAR images for the measurement of geophysical parameters and the generation of high-quality terrain maps using phase interferometry methods (Moreira et al., 2013). INSAR also uses the information from the phase difference between two SAR images to generate interferogram (Zebker & Goldstein., 1986). The key idea behind INSAR is to compare the phase of the given scene with two or more complex SAR images taken at different time intervals or from different positions (Moreira et al., 2013). The images are either acquired from mutually displaced flight tracks called across track interferometry or from one and the same flight track but at different times called differential interferometry.

The interferogram after co-registering the image is obtained by multiplying the pixels of image 1 (master image) and the conjugate of the pixels of image 2 (slave image) from which the phase can be extracted. The interferogram was first generated by Li & Goldstein (1990) using repeat-pass interferometry. This phase difference in images estimates the height location of local scatters. The interferometric phase and coherence are sensitive to spatial variability of vegetation height and density. This sensitivity at lower frequencies makes the estimation the vegetation parameters a challenge (Krieger et al., 2005). Numbers of applications in forestry like Mette et al. (2002) used volume de-correlation to extract forest height. It is also used to differentiate different types of forest for the estimation of biomass and forest height (Wegmüller & Werner, 1995). INSAR is mainly used for forest applications because it is sensitive to forest structure.

## 2.5 Forest height estimation techniques

Remote sensing has encouraged exceptional progress in displaying, mapping and understandings of the environment. Its application includes either image from the passive optical system, for example, airborne photography and Landsat Thematic Mapper (Goward & Williams, 1997) or to a lower degree of active sensors such as RADARSAT (Waring et al., 1995). These types of sensors have turned out to be suitable for numerous ecological applications, but the sensitivity and degree of precision tend to decrease with increasing above ground biomass and leaf index area (Turner et al., 1999). LIDAR (Light Detection and

Ranging) is a remote sensing technique that raises the efficiency of biophysical measurements of the forest. Various studies have been carried for estimation of the tree height in forest areas such as Nilsson (1996) used original extractor algorithm for tree height estimation. It has one disadvantage that in the case of more than four returns i.e. the ground surface reflection will not be detected. In addition to this, Suárez et al. (2005) developed an algorithm to provide a tree canopy model by extracting the high-resolution terrain model of the bare ground to estimate the individual tree height. Image segmentation and classification provide information about individual trees. In previous studies, it was found that in estimating aboveground biomass and carbon storage, the use of tree height is ignored so Feldpausch et al. (2012) incorporated forest height in biomass estimation. It increases the accuracy of biomass estimation. Further Hunter et al. (2013) assessed the impact of height measurement error on biomass estimation. Paris & Bruzzone (2015) proposed a 3-D model by fusing the low-density LIDAR data with high-resolution optical images for the estimation of tree top height. When it comes to spaceborne LIDAR, Gwenzi & Lefsky (2014) includes NDVI and interaction terms for the complex structure of savannas. The inclusion of these terms enhanced the canopy height modeling and also helpful in detecting height change. The integration of LIDAR data with optical remotely sensed data provides a cost cutting solution to the cost of LIDAR data (Ahmed et al., 2015). In this case, a machine learning approach is incorporated with the information from the analysis of time series of LANDSAT imagery for the calculation of forest structural parameters. Despite so many studies as stated above, for forest height measurement using LiDAR, it has several disadvantages like the spectrum used in LIDAR is infrared and cannot penetrate clouds. It is difficult to map features with LIDAR that follows edges because the LIDAR data have points placed on the landscape, not made to follow edges. In such scenarios, synthetic aperture radar plays an important role, and various researches have been carried for the estimation of forest parameters as Cloude & Papathanassiou (2008) developed an algorithm which is based on Polarization Coherence Tomography for vertical structure estimation. Also, to this Cloude et al. (2009) has used macro-ecology forest model coupled with coherence tomography for estimating vertical scattering profile. They also mentioned that structure has an impact on interferometric coherence and hence on forest height. Neumann et al. (2010) introduced a method by combining polarimetric decomposition with the random volume over ground (RVoG) model (Hongjun et al., 2007**)**. This full model uses the ground to volume ratio for estimating vertical forest structure parameters. It separates the interferometric coherence diversity and volume and ground coherency matrix based on polarization signatures resulting in enhancing the estimation of vertical forest structure. To dismiss the effect of temporal decorrelation Li et al. (2014) has proposed temporal de-correlation RVoG model with three stage inversion to estimate forest height. In addition to this, Chehade & Ferro-Famil (2013) estimated the forest height after separation of volume and ground contributions (Tebaldini, 2009). Praks et al. (2009) showed that high-frequency dataset also has good potential in height estimation. He experimented with X-Band data in the sparse forest, and it showed good potential in height

estimation. The experimental result showed that tree height can also be estimated by using one polarization interferometry. The change in height of the trees is related to the biomass is shown by Solberg et al. (2014). He used stereo imaging for tree height estimation. Reigber & Moreira (2000) showed the potential of SAR tomography and also highlighted the problem associated with SAR interferometry in measuring the tree height. This problem exists due to the distribution of scatter in height is underdetermined. Hagberg et al. (1995) found that coherence is insensitive to temporal changes like wind speed in repeat-pass SAR interferometry but sensitive to the temperature below zero degree. The tree height was estimated without concerning the amount of interferometric coherence but utilizing the assumption based on mean extinction (Garestier et al., 2008). His results also showed that height inversion was dependent on the density of sparse forest not on the frequency of the data. Balzter et al. (2007) introduced the use of dual wavelength for canopy height estimation. In addition to this, Cloude & Corr (2003) developed three height retrieval algorithms: Max differencing, full model inversion using two- layer coherence and vegetation bias removal algorithm. He found that vegetation bias gives better result in the presence of temporal effects, and full model inversion algorithm was more accurate in the absence of temporal effects. Lulu & Ruliang (2008) improved the estimation of volume decorrelation for improving the three stage inversion technique (Cloude & Papathanassiou, 2003). It results in the better estimation of tree heights. Chen et al. 2007 experimented with Three stage and ESPIRIT algorithm to extract the phase associated with ground and canopy component for estimating forest height and Lavalle et al. 2009 used coherence phase for the estimation of vegetated areas. Minh & Zou (2013) proposed a novel algorithm by removing the attenuation due to electromagnetic waves in the ground medium for the improvement in accuracy of tree height estimation. Chandola (2014) used three stage inversion algorithm to estimate tree height on POLINSAR data. In Three Stage Inversion technique by Cloude & Papathanassiou (2003), the inversion process can be performed after estimating the interferometric coherence value for different polarization channel and volume decorrelation. This volume decorrelation will be useful in determining the height of trees. Three stage inversion uses RVoG, which is a scattering model that gives effective ground to volume amplitude ratio (Hongjun et al., 2007). Coherency matrix plays an important role in the inversion process (Tan et al., 2009) of forest parameter extraction. Yamada et al. (2001) introduced ESPIRIT algorithm. This algorithm estimates the forest height by calculating the phase of each local scatters of the forest region. Coherence and phase diversity optimization remove the choice of polarization channels. It uses five optimum polarizations with three stage algorithm to estimate forest height (Xie et al., 2014).

# 3. Study area and Materials used

## 3.1 Barkot forest:

The study area comes under Dehradun Forest Division (DFD), situated in the Uttrakhand State of Northern part of India. It extends over an area of 454.95 km$^2$. There are eight ranges that come under Dehradun forest division Asarori, Malhan, Lachhiwala, Malsi, Jhanjara, Thano, Barkot, and Rishikesh. The DFD lies in Doon valley and surrounded by the Himalayas on the north, and the Shivalik ranges in the south. This shield the valley from heat and fragments from the plains making the forest moist. The classification of Champion & Seth (2005) divides the forest into Doon Valley Sal and Shivalik valley Sal. During 1950's and 60's, common forestry applications lead to the removal of miscellaneous species for thinning and maintenance of fire lines (Subudhi & Shah, 2009). Based on the forest policy in 1982, forestry operations were stopped, and the forest with only Sal was considered as managed forest and Sal with sub-dominant species were considered as a natural Sal forest. The reason for selecting the Barkot and Thano range are: they have almost flat topography, the major part of the ranges covered with homogeneous species of tree (Sal forest) and it is not necessary that the method applied on one forest range can be implemented on the other forest range so to test the potential of modelling approach these ranges are selected.

### 3.1.1 Thano range:

Thano range lies on the eastern side of the Dehradun forest division. It extends from 30.16° N to 30.31° N latitude and 78.13° E to 78.30° E longitude. The total area covered by Thano range is 11775 ha. The area is flanked by the adjacent forest of Barkot forest range in south and Lachhiwala Forest range in the west, Malsi forest range in northern and Pauri Garhwal and Tehri Garhwal hilly forests in the east. This area comprises of the natural forest ecosystem with pure Sal, and Sal dominated trees occupying a rough area of 3000 ha. Agricultural fields and human settlements along the side of Thano range put anthropogenic pressure on the forest that results in a different number of forest density classes. The division of Sal forest by (Champion & Seth, 2005) are as follows:

- Moist Shivalik Sal forest (3C/C2a)
- Moist Bhabar Dun Sal forest (3C/C2b9(i))
- Dry Shivalik Sal forest (5B/CIa)

The Moist Shivalik Sal forest subtypes are found in abundance followed by Moist Bhabar Dun Sal forest and a few patches of dry Shivalik forest. Thorny bushes of 'karaunda' *(Carissa opaca)* and 'kathber' *(Zizyphus*

*glaberrima)* restricted the growth of 5B/CIa subtype of Sal. Other types of forest other than Sal are named as Dry deciduous scrubs, Khair-sissoo, Northern dry deciduous and subtropical pine forest.

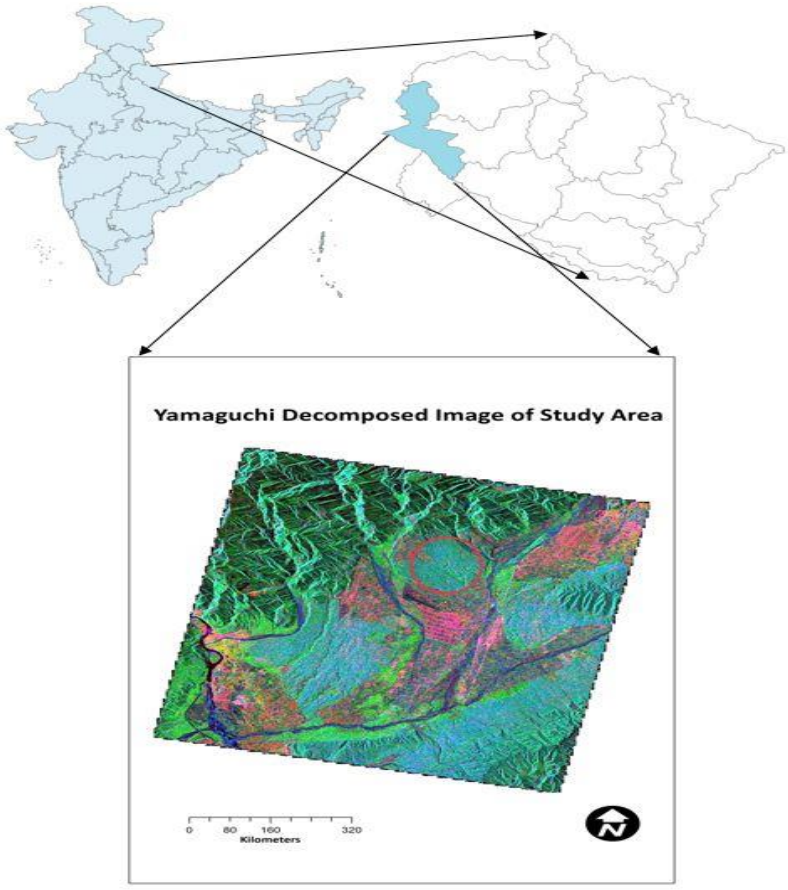


Figure 3.1 Location map of Thano Range

The climate of Thano range varies from sub-tropical to temperate, and the mean annual temperature is 20°. The area is mainly dominated by monsoon rain from July-September, and it is followed by short winter rainfall due to western disturbances from December to March. The mean annual rainfall of this area is 2080 mm (Singh, 2010).

### 3.1.2 Barkot range:

Another study area is Barkot Forest range located in the Uttrakhand state in the northern part of India, lies 40 km from Dehradun city in the southeast direction. It extends from 78.16° E- 78.28° E longitude and 30.06°-30.17° N latitude. Barkot range forest covers an area of around 11.5 kha out of which 7.1 kha of forest area comes under the reserved category. The area is flanked by Thano forest range in the north, Motichur forest range in the south and by Lachchhiwala forest range in the western part. The Dense forest

is found in the western part of the range which has a tree density of around 70 %. Sal *(Shorea Robusta)* is found in the major portion of the forest forming nearly pure stands. Sal forest is divided into Moist Shivalik Sal forest, Dry Shivalik Sal forest, and Moist Bhabar Doon Sal forest. Moist Shivalik Sal forest is the dominant species and is commonly observed in the forest. Apart from Sal other species are Teak (Tectona *grandis*), Rohini (*Mallotus philippensis (Lank) Muell. –Arg.*), Chamror (*Ehretia laevis Roxb.*), Sagaun (*Tectona grandis L.f*), Amaltash (*Cassia fistula L.*), Jamun (*syzgium Cumini (L.) skeels*) and Khair (*Acacia catechu (L.f.)*).

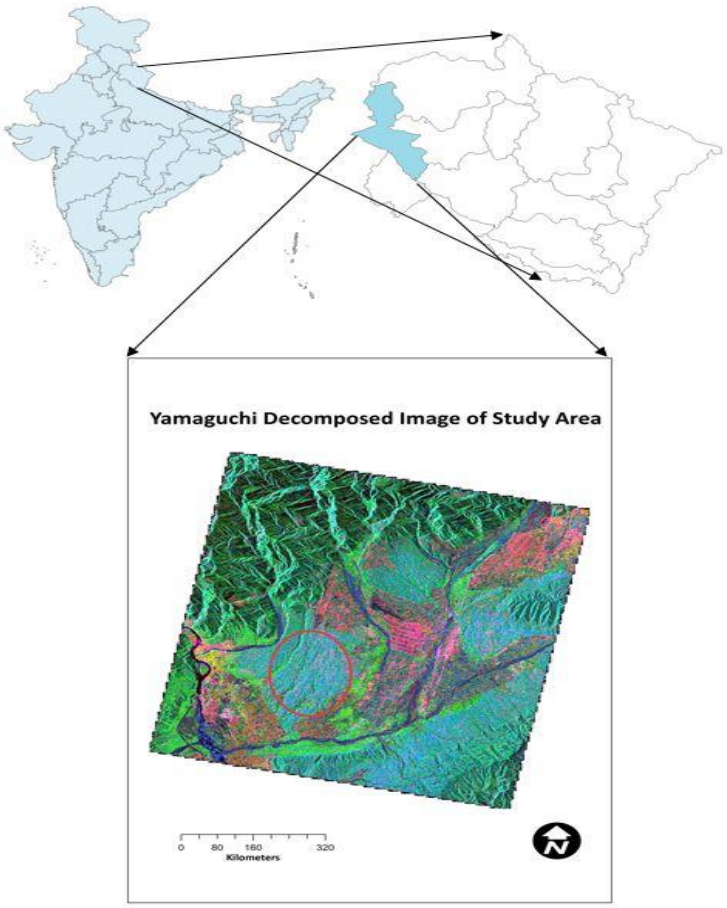


Figure 3.2 Location Map of Barkot Range

The annual temperature recorded by FRI (Forest Research Institute) Dehradun in the past 60 years is 20.4°C. The temperature in summer ranges from 23° C to 41° C and 5° C to 23° C in winter season. Rainfall is due to the monsoon which breaks out in the month of July and continue till the end of September. A very little amount of rainfall has been recorded from December to March due to western disturbances. Frost is common in winter season and cause damage to younger Sal trees.

## 3.2 Materials:

This section explains the satellite datasets, software, tools utilized and the information about the ground truth data collected for validation.

### 3.2.1 Satellite data:

An interferometric pair of fully polarimetric RADARAT-2 SAR data has been acquired for Thano and Barkot range forest to study the effect of Polarization Orientation Angle. This satellite has SAR sensor operating in C-band with data acquired in Fine Quad – polarization over a temporal baseline of 24 days that generate POLINSAR data pair. These datasets were acquired on 4th March 2013 and 28th March 2013 (Slave) also on 27th January 2014 (Master) and 20th February 2014 (Slave). It is in SLC (Single Look Complex) format where each pixel contains amplitude and phase information. Table 3.1 and Table 3.2 gives the details of the dataset used.

#### 3.2.1.1 Table for datasets used:

Table 3.1 Data characteristics of polarimetric interferometric data pair for 2013 and 2014

| **Description** | **Dataset 2013** | **Dataset 2014** |
|---|---|---|
| Number of images | 2 | 2 |
| Data Acquisition Date | 4-March-2013, 28-March-2013 | 27-jan-2014, 20 Feb-2014 |
| Band | C | C |
| Mode | Fine | Fine |
| Wavelength | 5.5 cm | 5.5 |
| Near incidence angle | 39.28 degree | 33.45 degree |
| Far incidence angle | 40.72 degree | 35.07 degree |
| Polarization | Quad-pol | Quad-pol |
| Normal baseline | 77.91 m | 67.92 |
| Critical baseline | 4743.30 m | 3850.61 m |
| Temporal baseline | 24 days | 24 days |

### 3.2.2 Software:

- Polarimetric SAR Data Processing and Education Toolbox (POLSAR pro v 5.2) (Institute of Electronics and Telecommunications of Rennes -University of Rennes, 2016) and Sentinel-1 Toolbox (S1TBX) developed by European Space Agency (2016) is used for software data processing.
- ArcGIS developed by ESRI is used for creating coherence height maps.

- ENVI 5.0 is used for the extraction and analysis of coherence and height values of forest stands from the SAR imagery. It is also used for the generation of vertical wave number file ($k_z$ file).
- R-software (RCoreTeam, 2015) is used to calculate the mean error and root mean square error (rmse**).**

### 3.2.3 Equipment:

Instruments required for ground surveys are:

- GPS for the collection of latitude and longitude information.
- Measuring tape.
- Forestry pro, a laser range finder with three points measuring capability useful for height measurement of trees.

### 3.2.4 Field survey:

A field survey was carried out in the month of January 2016 for the accuracy assessment of the results derived from the SAR data processing. Maps from the Uttrakhand Forest Department gave the details about the forest types and was helpful in planning the field data collection. As *in situ* data were available, so some data were collected based on the data availability and spatial coverage of tree species. The site was selected in such a way that it was possible to see the top and bottom of the tree.

Figure 3.3 Thano forest range comprising of Sal trees

The geo-location was obtained by Trimble Juno SB handheld GPS receiver. The positional error was observed between 7 m –-10 m. The tree height was obtained with the help of Forestry pro, a laser rangefinder instrument that uses three point measurement to calculate the tree height. Firstly the horizontal distance to the target is calculated then angle to the target base and the top. Once this three point measurement is achieved, the height of the tree is displayed on the screen. This instrument is accurate up to 0.5 m. 90 plots of 12.5 m × 12.5 m were taken in Barkot and Thano range. The average

height of trees in the plots along with the latitude and longitude position were measured. The field data details are tabulated in Appendix 1. Figure 3.3 shows the location of points obtained in Thano and Barkot ranges.

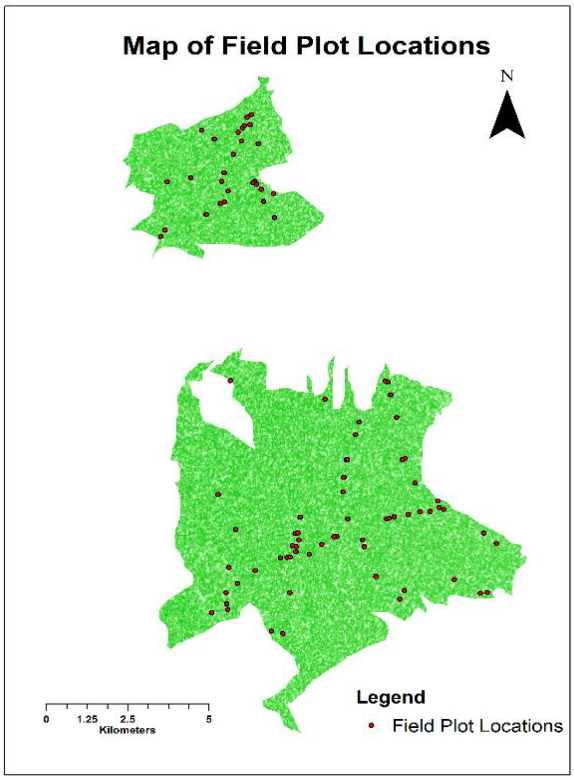


Figure 3.4 Field Plot locations in Barkot and Thano range

# 4. Methodology:

This chapter explains the step by step process to study the POA shift and POLINSAR based modeling for tree height estimation.

## 4.1 Generation of scattering matrix:

PolInSAR uses interferometry to combine two polarimetric images to form PolInSAR pair of images. These PolInSAR images are of the same area taken from slightly different angles at two different time periods. PolInSAR pair of images is useful in understanding the polarimetric and interferometric correlation that gives it an advantage over using simple polarimetry and interferometry techniques. From these two images, scattering matrix was generated.

$$[S_1] = \begin{bmatrix} S_{HH}^1 & S_{HV}^1 \\ S_{VH}^1 & S_{VV}^1 \end{bmatrix} \quad (4.1)$$

$$[S_2] = \begin{bmatrix} S_{HH}^2 & S_{HV}^2 \\ S_{VH}^2 & S_{VV}^2 \end{bmatrix} \quad (4.2)$$

where

1 and 2 define the superscripts.

## 4.2 Co-registration of master and slave images:

Since two images were taken from two different positions, so each pixel was aligned differently in both the images. The aim of the co-registration is to align the slave image with a master image in such a way that the co-registered image represents the same pixel as in the master image. The software used for co-registration was Sentinel-1 Toolbox (S1TBX).

There are two major steps in co-registration:

1. **Ground control points (GCP) selection:** In this process, GCP's of master image was generated and the GCP in slave image was computed based on the GCP of master image. These set of GCP's form a Warp function. This function creates a map between the pixel of master and slave images. After GCP selection, coarse registration is completed using the cross-correlation operation between the images. Cross-correlation defines the degree of similarity between the images. Finally fine registration was performed to maximize the complex coherence between the images.
2. **Warp operator:** It computes a polynomial of certain order once the valid number of master-slave GCPs pairs were available. Afterward, it maps the master GCPs onto the slave GCPs and at last co-registered image can be generated.

Temporal decorrelation exists due to the gap between the acquisitions of the two images. This temporal decorrelation results in loss of coherence. The loss of coherence is reduced by the process of co-registration.

### 4.3 Generation of coherency matrix [$T_6$]:

[$T_6$] matrix contains the polarimetric information as well as the information about the interferometric phase relation between the two images.

For the generation of 6x6 coherency matrix [$T_6$], coherent scattering vector $\underline{k}$ is utilized which is equivalent to the scattering matrix [S] vector (Cloude &Papathanassiou, 1998).

$$\underline{k} = \frac{1}{2}\, tr\big([S]\psi_p\big) \tag{4.3}$$

$$\underline{k} = \frac{1}{\sqrt{2}}\left[S_{HH} + S_{VV}, S_{VV} - S_{HH}, S_{VH} + S_{HV}, i(S_{HV} - S_{VH})\right]^T \tag{4.4}$$

where T indicates the transpose

$\psi_p$ is the orthogonal complex Pauli basis matrices

$$\psi_p = \left\{\sqrt{2}\begin{bmatrix}1 & 0\\ 0 & 1\end{bmatrix}, \sqrt{2}\begin{bmatrix}1 & 0\\ 0 & -1\end{bmatrix}, \sqrt{2}\begin{bmatrix}0 & 1\\ 1 & 0\end{bmatrix}, \sqrt{2}\begin{bmatrix}0 & -i\\ i & 0\end{bmatrix}\right\} \tag{4.5}$$

According to the reciprocity theorem, the scattering matrix becomes complex symmetric i.e. $S_{HV}=S_{VH}$. So the equation 4.4 becomes:

$$\underline{k} = \frac{1}{\sqrt{2}}\left[S_{HH} + S_{VV}, S_{VV} - S_{HH}, 2S_{HV}\right]^T \tag{4.6}$$

PolInSAR image is the result of two polarimetric images. $\underline{k}_1$ and $\underline{k}_2$ are the two coherent scattering vectors for the two scattering matrices.

$$\underline{k} = \begin{bmatrix}\underline{k}_1\\ \underline{k}_2\end{bmatrix} \tag{4.7}$$

where

$$\underline{k}_1 = \begin{bmatrix}S^1_{HH} + S^!_{VV}\\ S^1_{HH} - S^1_{VV}\\ 2S^1_{HV}\end{bmatrix} \tag{4.8}$$

$$\underline{k}_2 = \begin{bmatrix}S^2_{HH} + S^2_{VV}\\ S^2_{HH} - S^2_{VV}\\ 2S^2_{HV}\end{bmatrix} \tag{4.9}$$

where

1 and 2 are the superscripts

$[T_6]$ matrix can be defined as:

$$[T_6] = \langle \begin{bmatrix} \underline{k}_1 \\ \underline{k}_2 \end{bmatrix} \begin{bmatrix} \underline{k}_1^{*T} & \underline{k}_2^{*T} \end{bmatrix} \rangle = \begin{bmatrix} [T_{11}] & [\Omega_{12}] \\ [\Omega_{12}^{*T}] & [T_{22}] \end{bmatrix} \quad (4.10)$$

where

$$[T_{11}] = \langle \underline{k}_1 \, \underline{k}_1^{*T} \rangle \quad (4.11)$$

$$[T_{22}] = \langle \underline{k}_2 \, \underline{k}_2^{*T} \rangle \quad (4.12)$$

$$[\Omega_{12}] = \langle \underline{k}_1 \, \underline{k}_2^{*T} \rangle \quad (4.13)$$

$[T_{11}]$ and $[T_{22}]$ are the coherency matrices that contains polarimetric information.

$[\Omega_{12}]$ contains both polarimetric and interferometric information between the two images.

### 4.4 Orientation angle estimation:

There are various methods for the calculation of polarization orientation angle as explained in section 2.3. The circular polarization method gives the most accurate result (Lee et al., 2000). In this study, the circular polarization method is used for the calculation of orientation angle. The data compensated by the orientation angle improves the estimation of geophysical parameters.

Circular polarization method uses the phase difference between the left-left and right-right circular polarization (Lee et al., 2002):

$$S_{RR} = \frac{S_{HH} - S_{VV} + i2S_{HV}}{2} \quad (4.14)$$

$$S_{LL} = \frac{S_{VV} - S_{HH} + i2S_{HV}}{2} \quad (4.15)$$

The orientation angle is computed using either single look complex or multi-look data by the angle of correlation between $S_{RR}$ and $S_{LL}$ (Lee et al., 2000).

$$\theta = [Arg(\langle S_{RR} S_{LL}^{*} \rangle) + \pi]/4 \quad (4.16)$$

From equation 4.16 the OA can be written as (Lee & Ainsworth, 2011):

$$\tan(-4\theta) = \frac{-4Re(\langle(S_{HH} - S_{VV})S_{HV}^*\rangle)}{-\langle|S_{HH} - S_{VV}|^2\rangle + 4\langle|S_{HV}|^2\rangle} \quad (4.17)$$

The inclusion of $\pi$ in the above equation is for the extraction of useful information related to building alignment and surface slopes in the azimuth direction. The above equation is modified to

$$\eta = \frac{1}{4}\left[\tan^{-1}\left(\frac{-4Re(\langle(S_{HH} - S_{VV})S_{HV}^*\rangle)}{-\langle|S_{HH} - S_{VV}|^2\rangle + 4\langle|S_{HV}|^2\rangle}\right) + \pi\right] \quad (4.18)$$

where

$$\theta = \begin{Bmatrix} \eta, if\ \eta \leq \frac{\pi}{4} \\ \eta - \frac{\pi}{2}, if\ \eta > \frac{\pi}{4} \end{Bmatrix} \quad (4.19)$$

### 4.5 Orientation angle shift on POLINSAR data:

In PolInSAR data, the main observable is the 6x6 coherence matrix [$T_6$] that contains polarimetric and interferometric information but for the calculation of orientation of an object only the polarimetric radar data is used (Lee et al., 2002). Thus, 6x6 coherence matrix is not compensated for the induced shift. Since scattering matrix contains the polarimetric information about the various scatter within an SAR resolution cell, so it is used for the compensation of induced shift in POA for the two acquisitions. The following equation derives the compensated scattering matrix [$\bar{S}$] (Lee et al., 2002).

$$[\bar{S}] = [U][S][U] \quad (4.20)$$

$$[\bar{S}] = \begin{bmatrix} \cos\theta & \sin\theta \\ -\sin\theta & \cos\theta \end{bmatrix} \begin{bmatrix} S_{HH} & S_{HV} \\ S_{VH} & S_{VV} \end{bmatrix} \begin{bmatrix} \cos\theta & -\sin\theta \\ \sin\theta & \cos\theta \end{bmatrix} \quad (4.21)$$

where

$[S]$ is the scattering matrix before the compensation

$[\bar{S}]$ is the compensated scattering matrix

$[U]$ is the unitary rotation operator

The compensated scattering matrix is generated for both the images after POA compensation.

Pauli basis matrices can decompose the scattering matrix and easily derived the rotation in circular polarization. The scattering mechanism is better described by the Pauli basis vector as it is closely related to the physics of wave scattering. The rotation of target vector of Pauli matrices can be described as(Lee et al., 2002):

$$\bar{k} = U\underline{k}\ with\ U = \begin{bmatrix} 1 & 0 & 0 \\ 0 & \cos 2\theta & \sin 2\theta \\ 0 & -\sin 2\theta & \cos 2\theta \end{bmatrix} \qquad (4.22)$$

New compensated $[\overline{T_6}]$ coherency matrix is generated from the new target vectors $\overline{k_1}$ and $\overline{k_2}$. Now the height and coherence is generated from the new compensated $[\overline{T_6}]$ coherency matrix.

### 4.6 Flat earth removal:

The near to far range of each image acquired by separating the two antennas in space i.e. spatial baseline is affected by the variation of the phase of the returned signal. The flat earth removal removes the phase variation leaving only phase difference information associated with the height of the object present on the ground. It also involves the removal of the signal from the flat scene.

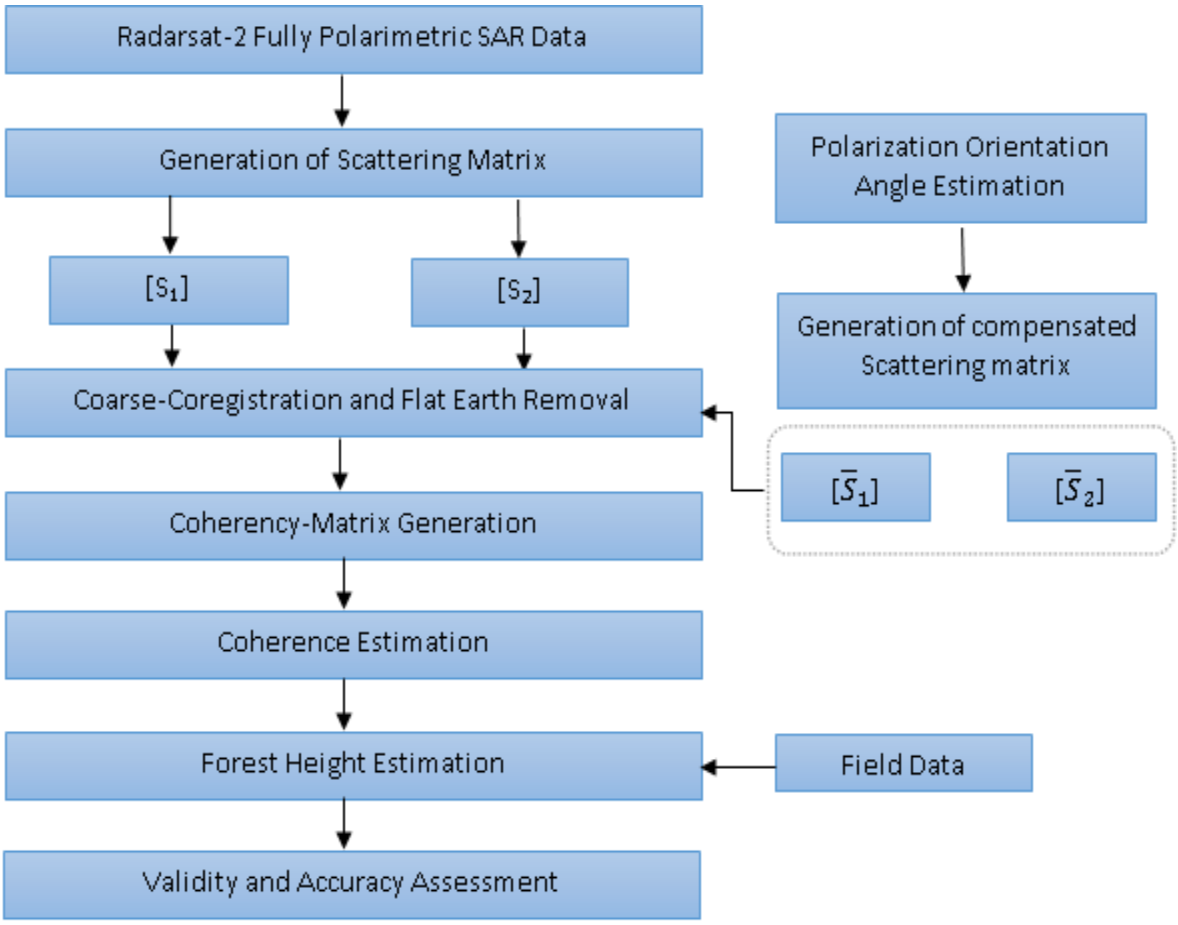


Figure 4.1 Methodology flow chart for the study of POA shift and tree height retrieval on PolInSAR data

### 4.7 Coherence estimation:

Coherence can be defined as the magnitude normalized cross-channel correlation between the two signals that was obtained from two spatially separated antennas. Coherence magnitude map is used for target classification. The black portion of the image shows low coherence and white portion shows the high value of coherence. The degree of coherence is measured by absolute coherence whose values ranges from 0 to 1 where 0 denotes complete decorrelation, and 1 denotes pure target with complete correlation. The coherence value 1 is mainly observed in urban areas whereas there is always lower coherence found in the forest areas. In interferometry, coherence phase from coherence magnitude map is used to extract the information about the target height or displacement (Touzi et al., 1999).

The interferometric coherence can be defined as (Cloude & Papathanassiou, 1998):

$$\gamma_{int} = \frac{|\langle s_1 s_2^* \rangle|}{\sqrt{\langle s_1 s_1^* \rangle \langle s_2 s_2^* \rangle}} \qquad (4.23)$$

where $0 \leq \gamma \leq 1$

<..> indicates the expectation value.

where $s_1$ and $s_2$ are the two complex signals.

Two complex vectors $\underline{w}_1$ and $\underline{w}_2$ were used to extend the scalar formulation into vectorial one.

Scattering coefficient $\mu_1$ and $\mu_2$ were generated as follows:

$$\mu_1 = \underline{w}_1^{*T} k_1, \quad \mu_2 = \underline{w}_2^{*T} k_2 \qquad (4.24)$$

$\mu_1$ and $\mu_2$ are the scaler functions of the linear combination of the elements of scattering matrices and form the basis of vector interferogram.

Now by combining equation (4.13) and (4.24) the expression for vector interferogram can be defined as:

$$\mu_1 \mu_2^* = \left(\underline{w}_1^{*T} \underline{k}_1\right)\left(\underline{w}_2 \underline{k}_2^{*T}\right) = \underline{w}_1^{*T} [\Omega_{12}] \underline{w}_2 \qquad (4.25)$$

The complex coherence is formed after vectorization of the interferometric coherence and the general vector expression for coherence is (Cloude & Papathanassiou, 1998):

$$\gamma = \frac{\left|\langle \underline{w}_1^{*T} [\Omega_{12}] \underline{w}_2 \rangle\right|}{\sqrt{\langle \underline{w}_1^{*T} [T_{11}] \underline{w}_1 \rangle \, \langle \underline{w}_2^{*T} [T_{22}] \underline{w}_2 \rangle}} \qquad (4.26)$$

where <…> expectation value

### 4.8 Vertical wave number and baseline Simulation:

The decorrelation increased with increase in baseline known as baseline decorrelation error. Prati et al. (1990) shown that baseline decorrelation reached in correspondence with the critical baseline. In spectral approach, the spectrum of signals from two images defines the ground reflectivity spectrum for different bands and can be demonstrated by the relation between frequency f and ground wave-number $k_y$ (Prati et al., 1994):

$$k_y = \frac{4\pi}{\lambda} \sin(\theta - \alpha) \tag{4.27}$$

where

$k_y$ is the ground range wave-number

$\alpha$ is the slope of the terrain

When radar images the area, the slight change in looking angle $\Delta\theta$ generates a shift $\Delta k_y$ i.e. variation of $k_y$ and can be defined as (Kugler et al., 2015)**:**

$$\Delta k_y = \frac{4\pi f_0 \Delta\theta}{c} \cos(\theta - \alpha) \tag{4.28}$$

The ground wave number shift is changed to equivalent frequency shift Δf for comparing the shift in ground reflectivity to the SAR bandwidth W. This expression can be defined by differentiating equation (4.27) (Gatelli et al., 1994):

$$\Delta f = -\frac{f_0 \Delta\theta}{\tan(\theta - \alpha)} = -\frac{cB_n}{r_0 \lambda \tan(\theta - \alpha)} \tag{4.29}$$

where

$\alpha$ is the terrain slope

$r_0$ is the sensor target distance

$B_n$ is the normal baseline

$\lambda$ is the wavelength

The above expression explains that spectral component of one signal is shifted by Δf in the other signal when the signal from two SAR measurements differ by a slight change in angle Δθ. Since single SAR resolution cell contains a large number of scatters then the scatter from two images with different elevation z have a wave number in elevation. This wave number is known as vertical wavenumber and show the shift of scatter in elevation by a slightly change in look angle during imaging by radar. The vertical wave number has the following form:

$$k_z = \frac{2\omega}{c} \cos\theta \tag{4.30}$$

To observe same $k_z$ from two images, the change in looking angle is compensated by spectral shift of $\Delta\omega = -\ \omega\Delta\theta/\tan\theta$ which is equivalent to $k_z$ wave number shift.

$$\Delta k_z = \frac{2\omega\Delta\theta}{c\sin\theta} \tag{4.31}$$

The degree of correlation between $k_z$ and $k_z$ and $\Delta k_z$ affects the coherence values.

The vertical wave number $k_z$ depends on the incidence angle and range component of terrain slope.

The generation of vertical wave number is crucial for tree height estimation. The dependency of the baseline on vertical wave number results in effectiveness of the tree height. The vertical wave number depends on baseline according to the following formula (Cloude, 2005):

$$k_{z=}\frac{4\pi B_n}{\lambda H\tan\theta} \tag{4.32}$$

where

H is altitude,

$\lambda$ is the wavelength,

$B_n$ is the minimum baseline.

Here the value of $k_z$ depends on baseline i.e. increase in baseline increases the value of $k_z$ and vice-versa. The compensation of non-volumetric decorrelation contributions depends on the choice of appropriate vertical wave number. In studies, it was found that single value of $k_z$ results in inversion for a limited range of forest heights. For a wide range of forest height, the multiple POLINSAR acquisitions with different $k_z$ values are required. It plays an important role in the inversion performance of POLINSAR for the forest height estimation. The large value of $k_z$ saturates the sensitivity of coherence to forest height and results in underestimated of larger heights. On the other hand, the low value of $k_z$ introduces large height error due to unfavorable coherence to height scaling (Kugler et al., 2015). So the choice of correct baseline is important here. According to Wang (2006), the height measurement sensitivity increases when baseline increases. It also decreases the correlation between the two images, so the increase in baseline beyond some value will results in decreases in accuracy of height measurement. So the optimal baseline is required to balance these two opposing factors.

Another factor that plays an important role in correct height estimation is the height of ambiguity. It can be defined as the height that generates the interferometric phase change of $2\pi$. The height of ambiguity can be written as (Krieger et al., 2007):

$$z_{min} = \frac{R\lambda\ \sin\theta}{2\ B_n} \tag{4.33}$$

where

$B_n$ is the minimum baseline

$\theta$ is incidence angle,

R is distance from sensor to target

The above equation shows that baseline is inversely proportional to the height of ambiguity i.e. increase in baseline decreases the height of ambiguity that gives less change in phase between the two images. The result is less de-correlated images with estimated height tending towards the true value (Sefercik & Dana, 2008).

According to Steinbrecher et al. (2013) to avoid superposition of replicas the height of ambiguity should be greater than the tree height i.e. the maximum tree height of 27 m can be unambiguously resolved if the height of ambiguity is more than 27 m. In this research, the maximum tree height obtained in the forest as ground truth is 29 m, so the baseline is simulated according to the height of ambiguity of 30 m for the correct estimate of tree height.

### 4.9 Modeling for the estimation of tree height:

POLINSAR is a precise technique in extracting the vertical structure information of forest. This technique uses different polarization combinations to generate phase differences between interferograms. The correction of these phase differences which are correlated with vegetation height gives accurate estimates of height (Cloude & Papathanassiou, 2003). The main application for wave scattering model is the inversion of ground scatter parameters in vegetated areas. For this, different wave scattering models are introduced. The dependency of wave extinction on polarization divide the scattering models in two categories: Random Volume (RV) and Oriented Volume (OV) scattering model which are further classified as: random volume scattering model (RV), random volume over ground (RVoG) scattering model, oriented volume (OV) scattering model, oriented volume over ground (OVoG) scattering model (Hongjun et al., 2007).

These models relate observation to vegetation parameters.

**Random volume (RV) scattering model**: models the vegetation layer with a thickness $h_v$ having a volume of randomly oriented particles. The randomly oriented particles in the volume of a tree are defined by random orientation. These particles propagate through the volume or canopy of a tree independent of the polarization state of the wave that makes the distribution of scatterers in vertical direction stable with polarization. In random volume scatter model the ground scatterer is ignored. The interferometric coherence can be written as: (Papathanassiou & Cloude, 2016).

$$\tilde{\gamma}_{RV} = exp(j\varphi_0)\tilde{\gamma}_v \qquad (4.34)$$

where

$\varphi_0$ ground topographic phase,

$\tilde{\gamma}_v$ volume only complex coherence.

This volume only coherence depends on thickness $h_v$ and extinction coefficient and can be defined as:

$$\tilde{\gamma}_v = \frac{I}{I_0}, \begin{Bmatrix} I = \int_0^{h_v} e^{\frac{2\sigma z'}{\cos\theta}} . e^{ik_z z'} dz' \\ I_0 = \int_0^{h_v} e^{\frac{2\sigma z'}{\cos\theta}} dz' \end{Bmatrix} \qquad (4.35)$$

where

$\sigma$ is the wave mean extinction

$k_z$ is the vertical wave number

$\theta$ is the mean angle of incidence

**Oriented volume:** Unlike RVoG, the particles in the volume of the oriented volume scattering model are oriented and makes the wave to propagate with different complex wave numbers at different polarizations. Here eigenpolarizations describe the wave propagation through the oriented volume. The change in wave extinction coefficient changes the polarization of vertical distribution of scatters thus makes the coherence a function of polarization and can be defined as (Hongjun et al., 2007).

$$\tilde{\gamma}_{OV}(\vec{\omega}) = exp(j\varphi_0)\tilde{\gamma}_v(\vec{\omega}) \qquad (4.36)$$

with

$$\tilde{\gamma}_v(\vec{\omega}) = \left\{ \frac{\int_0^{h_v} e^{\frac{2\sigma(\vec{\omega})z'}{\cos\theta}} . e^{ik_z z'} dz'}{\int_0^{h_v} e^{\frac{2\sigma(\vec{\omega})z'}{\cos\theta}} dz'} \right\} \qquad (4.37)$$

where

$\theta$is the mean angle of incidence

$k_z$ is the vertical wave number

$\sigma(\vec{\omega})$ is the extinction coefficient

The phase center moves towards the top of the volume with increasing extinction, thus increasing the interferometric coherence.

**Oriented volume over ground:** In this scattering model, volume complex coherence is the function of polarization. It includes the contribution from ground and volume scatterers. Now the coherence from both ground and volume becomes the function of polarization i.e. the distribution of scatterer within the ground and volume scattering component changes with polarization. There are two parameters that are

dependent on polarization: extinction coefficient and ground to volume amplitude ratio. The coherence for OVoG model can be defined as (Papathanassiou & Cloude, 2016).

$$\overrightarrow{\gamma}_{OVoG}(\vec{\omega}) = e^{i\phi_0}\frac{\tilde{\gamma}_v(\vec{\omega}) + m(\vec{\omega})}{m(\vec{\omega})} \tag{4.38}$$

where

$m(\overrightarrow{\omega})$ is the ground-to-volume amplitude ratio.

**Random volume plus ground model:** This model also considers the ground scatter for the inversion process. It is useful with the band having a high wavelength or low frequency such as L, P and C bands that can penetrate the canopy of a tree giving ground and double-bounce scattering. It modeled the vegetation with a layer of thickness $h_v$ located over a ground scatter with scattering amplitude $m_g$. Usually, it is found that the canopy extends from crown to ground. In such cases, the RVoG model is a two-layer model. Since there are different varieties of vegetation, exist depending upon the significant species and age-related variations (like pine), so the two layer RVoG model is changed to three layer model with an extra phase parameter. The purpose of this is to ground phase point away from the canopy.

The RVOG model defines coherence as (Kugler et al, 2015):

$$\bar{\gamma}(\underline{w}) = e^{i\varphi(z_0)}\left(\bar{\gamma}_{v0} + \frac{\mu(\underline{w})}{1+\mu(\underline{w})}(1-\bar{\gamma}_{v0})\right) \tag{4.39}$$

Or

$$\bar{\gamma}(\underline{w}) = e^{i\varphi(z_0)}\left(\bar{\gamma}_{v0} + F(\underline{w})(1-\bar{\gamma}_{v0})\right) \tag{4.40}$$

where

$\underline{w}$ is a unitary vector that defines the polarization

$\bar{\gamma}_{v0}$ is the volume coherence

$\varphi(z_0)$ is the phase related to the ground topography,

$\mu$ is the effective ground to volume scattering ratio.

$F(\underline{\omega})$ lies in the range $0 \leq F(\underline{\omega}) \leq 1$ with $\mu=0$ for pure volume scattering and $\mu = \infty$ for pure surface scattering.

$\mu$ is the only parameter that changes with polarization channel. Here there is no monotonicity exist between coherence amplitude with increasing $\mu$. The tree canopy contributes to volume scattering, and HVpVH polarization channel defines the good approximation to volume scattering. For pure volume scattering the value of $\mu$ is zero ($\mu=0$). The cross-polarized channel (HVpVH) have low surface to volume scattering ratio with high phase center (Cloude, 2005).The selection of HVpVH polarization channel gives

minimum value of μ which results in minimum coherence except when $F_{min}$ is greater than zero. $F_{min}$ can be obtained by calculating minima for the above equation (4.40) and can be written as (Cloude, 2010):
if $F_{min} > 0$ then

$$\mu_{min} = 10\, log_{10}\left(\frac{\left|\bar{\gamma}_{v0}{}^{2}\right| - Re(\bar{\gamma}_{v0})}{1 - Re(\bar{\gamma}_{v0})}\right) \qquad (4.41)$$

This $F_{min}$ function is for both coherence amplitude and phase.

In RVOG model, the coherence and phase are not independent quantities as it assumes an exponential structure function in the volume. Cloude (2010) concluded that there is always some mixture of surface and volume that gives minimum coherence and μ =0 never gives minimum coherence. This is the weakness of the RVOG model. This weakness is removed by structured volume over ground model (SVOG) model by changing the relationship between the coherence amplitude and phase of the volume only at μ =0 point. The relationship between coherence amplitude and phase is no longer restrictive as a result of which the minimum coherence is the volume only coherence. This model is a three layer model with a layer of the volume, surface reflection from a position separated by a gap from this volume, scattering from the top layer can be shown below:

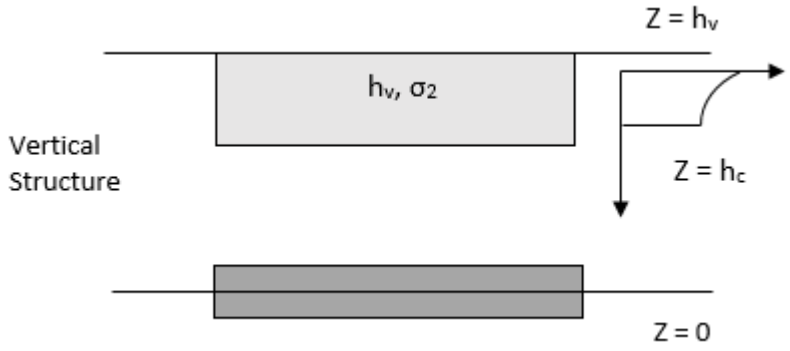


Figure 4.2 Structured volume over ground model

Here the phase will be large and the value of coherence amplitude of volume only channel will be small. This structured modelling is used in Coherence Amplitude Inversion.

### 4.10 Coherence amplitude inversion:

As it was mentioned earlier that that selection of HVpVH polarization channel gives minimum coherence amplitude. In low coherence regions, there is an ambiguity between the two intersection points on the unit circle which results in two heights at the same point. To remove these errors, one method is to isolate the points which give ambiguous heights by checking the solutions on both intersection point or employ height estimation algorithm. One such algorithm is Coherence Amplitude Inversion algorithm. Coherence Amplitude Inversion selects the polarization with a low surface to volume scattering ratio by ignoring the

phase completely and taking coherence amplitude only into consideration. This coherence amplitude is compared with random volume prediction to estimate height. The coherence height can be estimated by using the following equation (Cloude, 2005):

$$\min L_1 = \left\| \left| \tilde{\gamma}_{\underline{\omega}_v} \right| - \left| \frac{P\, e^{p_1 h_v} - 1}{p_1 e^{p_1 h_v} - 1} \right| \right\| \tag{4.42}$$

where

$$p = \frac{2\bar{\sigma}}{\cos\theta}$$

$$p_1 = p + ik_z, k_z = \frac{4\pi\Delta\theta}{\lambda \sin\theta} = \frac{4\pi B_n}{\lambda R \sin\theta}$$

# 5. Results and Discussion

This chapter includes the results that were obtained using PolInSAR data processing and field data. The tree height is estimated using Coherence Amplitude Inversion algorithm and the accuracy assessment for tree height has been done using field data. The effect of POA shift on the estimated tree height has also been included in this chapter. It includes result from the two different datasets taken in 2013 and 2014.

## 5.1 Coherence in Pauli basis for 2013

Coherence is generated by using equation 4.26

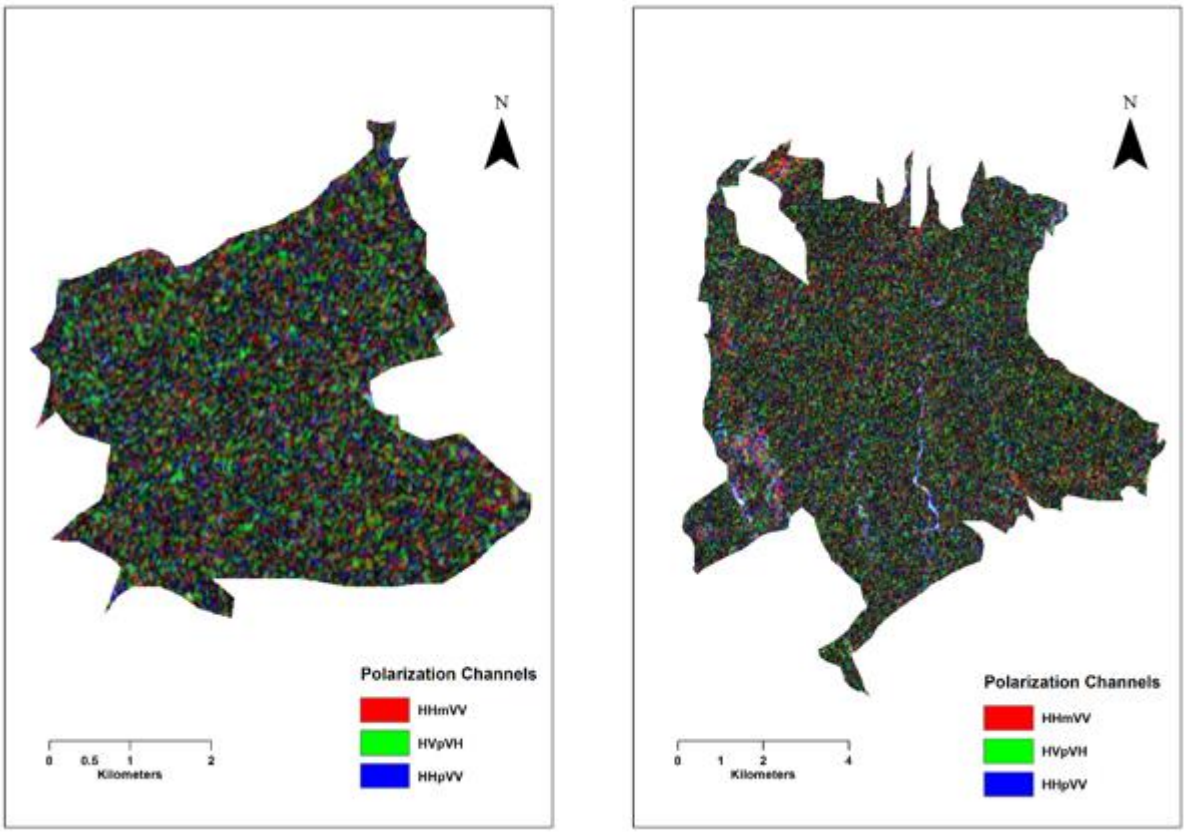


Figure 5.1 Color composite map of Thano range (left) and Barkot range (right) before POA compensation for 2013

The color composite map provides a better visual interpretation of the coherence. It was observed from the maps that the dry river bed regions were very bright which indicates the presence of very high coherence in all the three polarization channels. The brightness occurs due to the presence of closely spaced big stones which contribute to all types of scattering and also dry river bed does not change with time which leads to low temporal decorrelation.

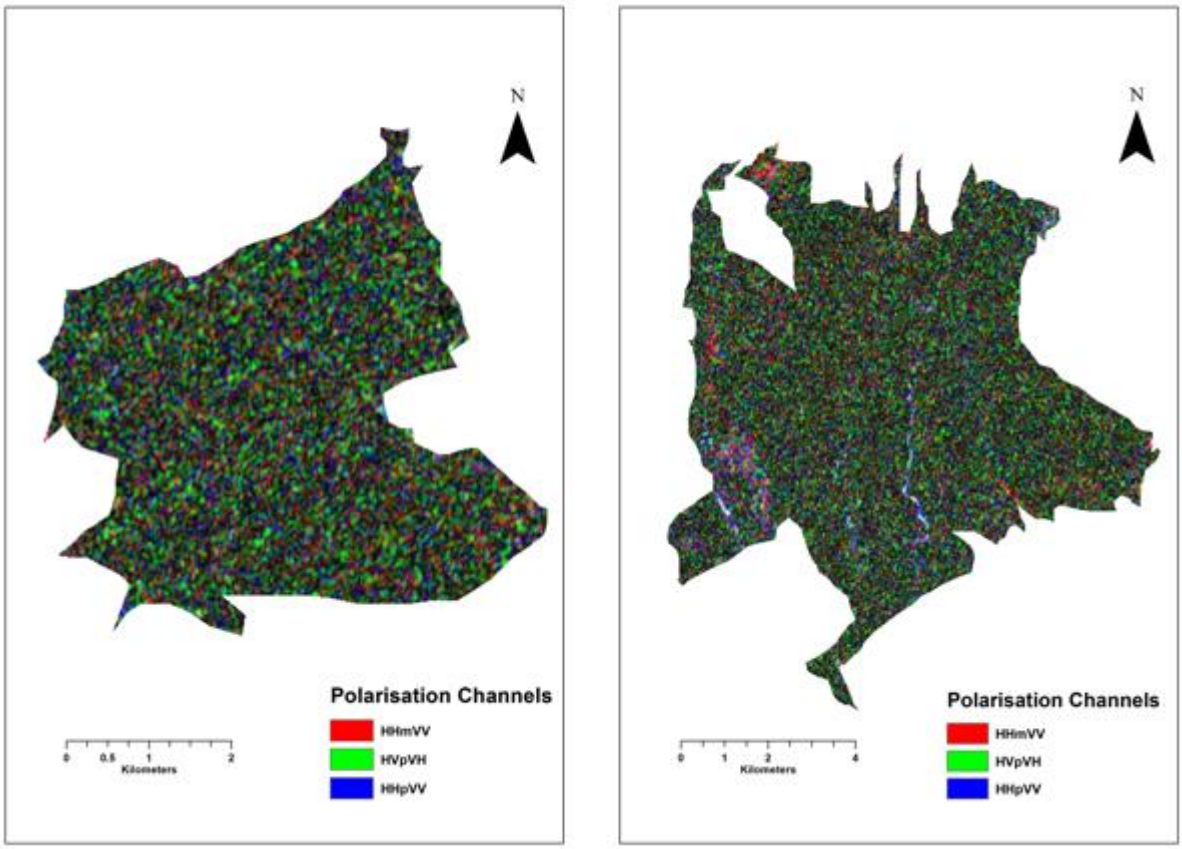


Figure 5.2 Color composite map of Thano range (left) and Barkot range (right) after POA compensation for 2013

Cyan color in dry river bed represents double bounce scattering due to the presence of big stones and surface scattering because of the ground surface. Forest area of Thano and Barkot ranges appears in green color and contributes to lower coherence values due to the presence of temporal decorrelation. Some areas in Barkot and Thano ranges shows reddish and bluish color. In these regions trees are thinly distributed that gives rise to double bounce scattering and surface scattering. The region showed in fig 5.2 in the southwestern part of Barkot range gives reddish color due to the presence of a bridge on the road that contributes to double-bounce scattering.

## 5.2 Coherence in Pauli basis for 2014 dataset

The color composite image of coherences for dataset 2014 is shown in Fig. 5.3

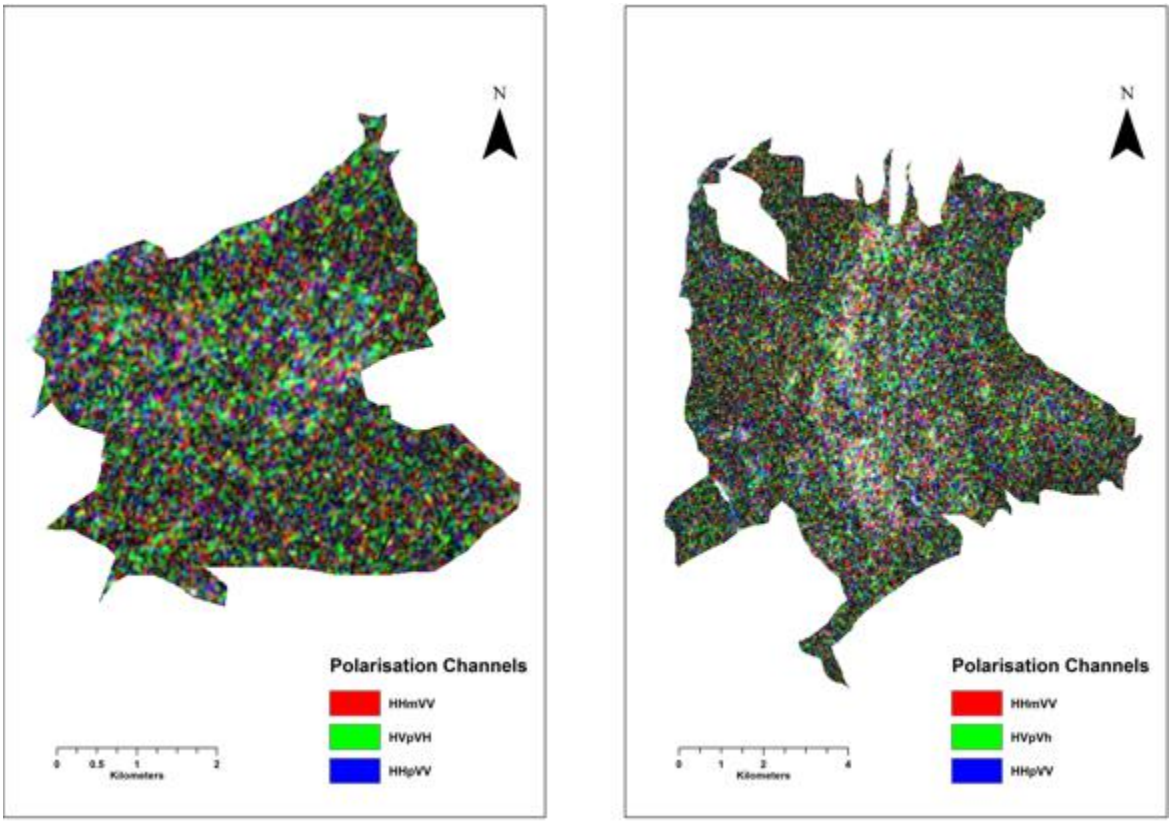


Figure 5.3 Color composite map of Thano range (left) and Barkot range (right) after POA compensation for 2014

Fig. 5.3 is brighter than Fig. 5.2 because of lower incidence angle in Fig. 5.3. The lower the incidence angle has more backscatter information as compared to the high incidence angle. In the case of high incidence angle, the waves interact with the top of the canopy which is not stable scatterer results in decrease in coherence values whereas for lower incidence angle, the waves interact with the top of the canopy as well as with the bottom of the tree through canopy gaps results in increased coherence values.

### 5.3 Coherence analysis before and after POA compensation for 2013

The graph for the volume scattering for dataset 2013 is shown in Fig. 5.4

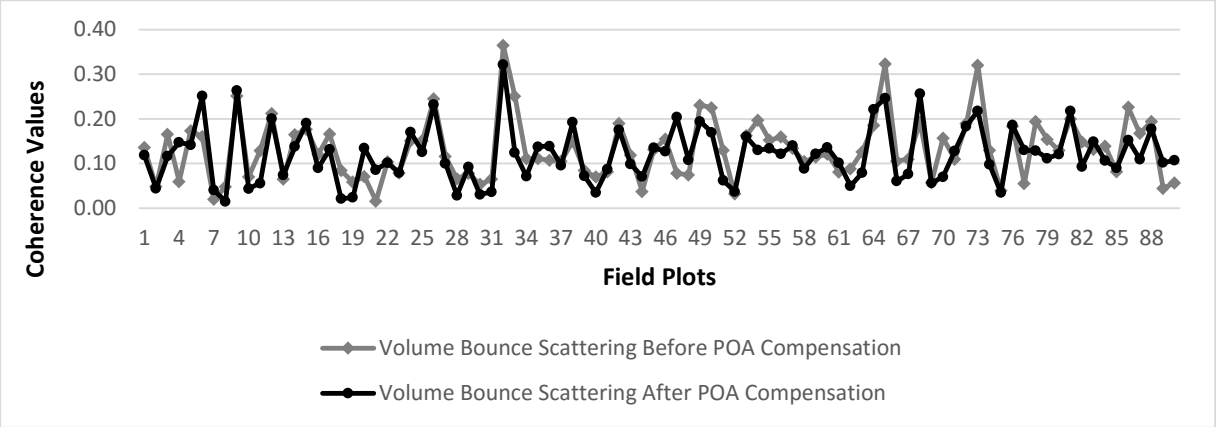


Figure 5.4 Volume scattering before and after POA compensation for 2013

The graph for the dry river bed region of dataset 2013 is shown in Fig. 5.5

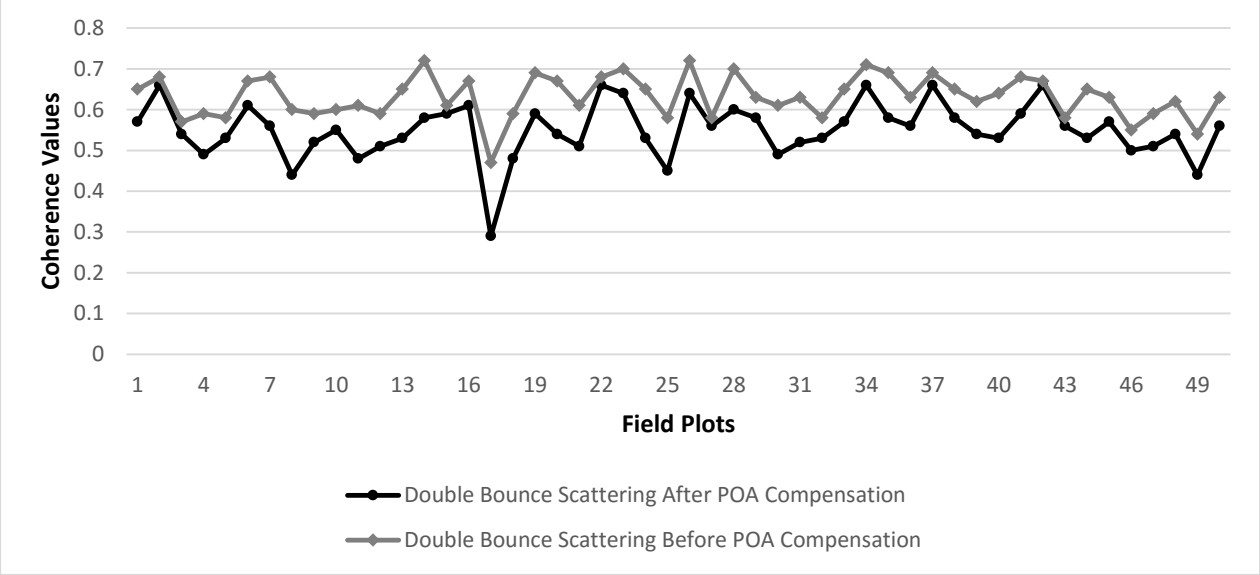


Figure 5.5 Double bounce scattering before and after POA compensation for 2013

## 5.4 Coherence analysis before and after POA compensation for 2014

The graph for the volume scattering for dataset 2014 is shown in Fig. 5.6

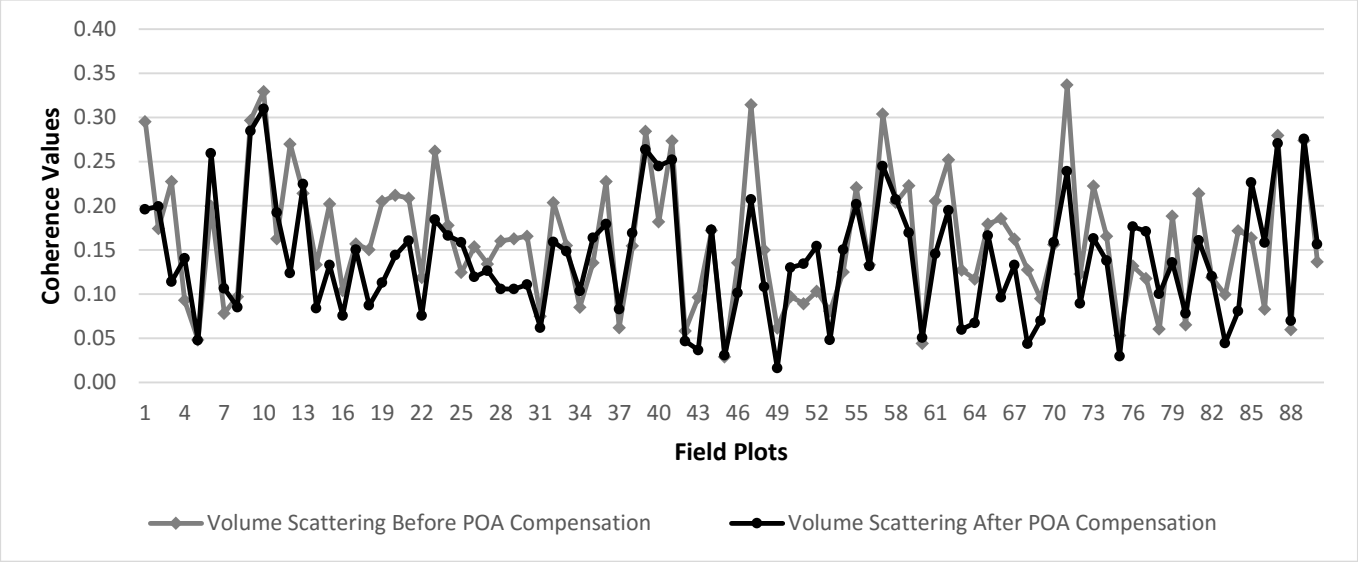


Figure 5.6 Volume scattering before and after POA compensation for 2014

The graph for the dry river bed region of dataset 2014 is shown in Fig 5.7

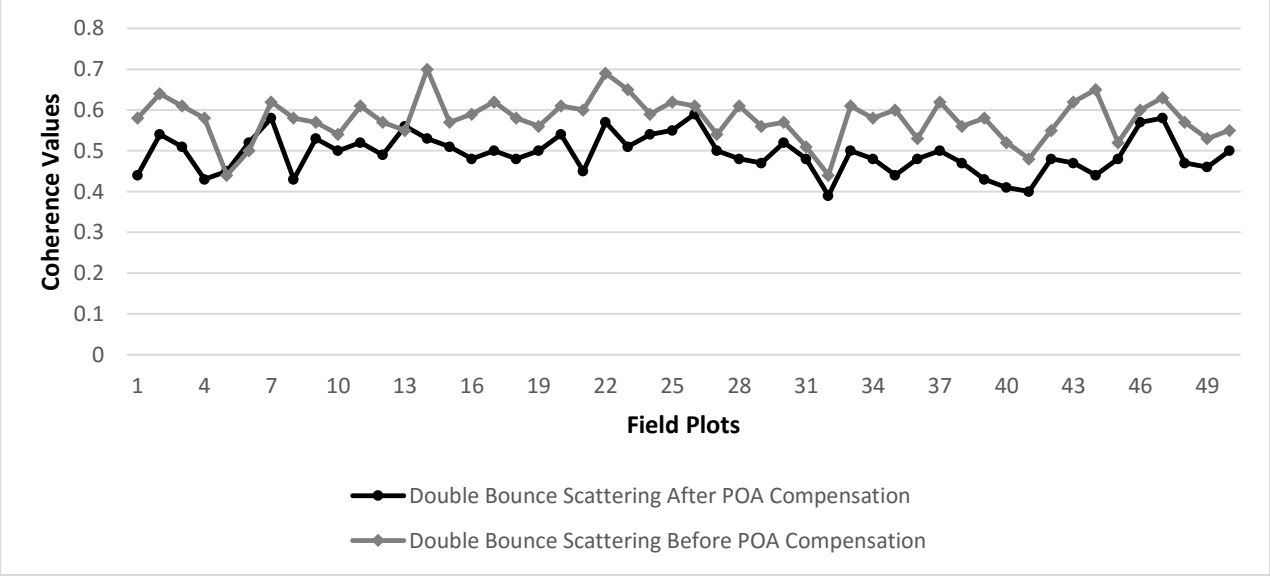


Figure 5.7 Double bounce scattering before and after POA compensation for 2014

## 5.5 Fieldwork results

The height measurement was taken for 90 plots, and it ranges from 15 m to 29 m with an average height of 23.62 m.

## 5.6 Coherence amplitude inversion height

Tree height has been estimated using coherence amplitude inversion technique. This technique was used as explained earlier in section 4.10. It takes coherence amplitude into consideration and for a known extinction in the layer, it calculates the height by using the relation between the height and coherence. It requires the selection of two polarization channels, one with volume scattering and other with surface scattering. Here HVpVH is selected for the volume scattering, and HHpVV is selected for the surface scattering.

## 5.7 Forest height map of dataset 2013 before POA compensation

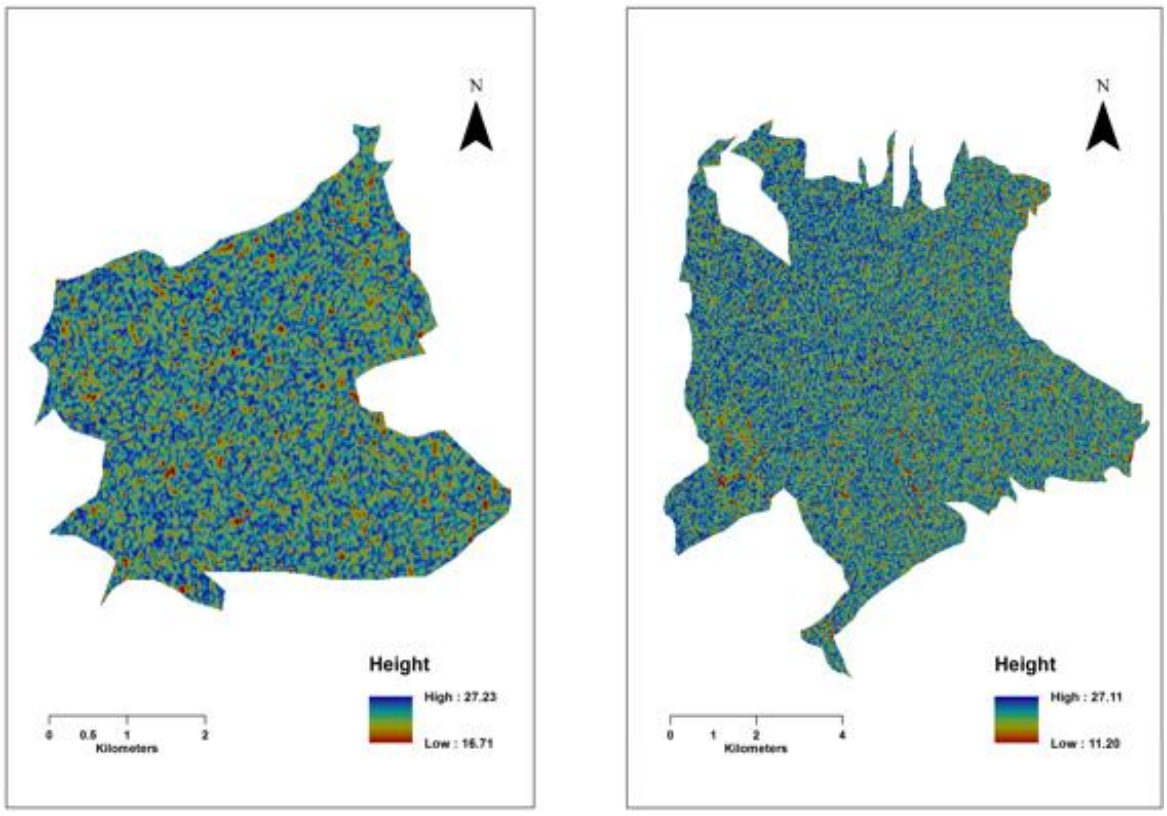


Figure 5.8 Tree height map of Thano range (left) and Barkot range (right) before POA compensation for 2013

## 5.8 Validation and accuracy assessment for the year 2013 before POA compensation

The field height is validated against the modeled height over 90 locations comprises of Barkot and Thano range.

Table 5.1 Table shows the data statistics for 2013 before POA compensation

| Forest Height Using | Sample Plot | Mean Height | Min Height | Max Height | Significance (p-value) |
|---|---|---|---|---|---|
| Field Data | | 23.79 | 16.60 | 29 | 0.18 |
| Coherence Amplitude Inversion | | 23.91 | 19.06 | 26.79 | 0.01 |

The accuracy obtained is 88.88 % with RMSE of 3.17 m.

Shapiro-Wilk test to check the normality of the data is used. For the 95 % of the confidence interval, the p-value is the significance value for passing the normality test. If the p-value is greater than 0.05, it will be assumed that tree height plots are a part of the normally distributed population.

Since the p-value for field data is greater than 0.05, it means that the field data is a part of the normally distributed population. For CAI the p-value is less than 0.05, it means that the CAI height plots are not a part of the normally distributed population.

The scatter plot shows the comparison of field data with the measured data. The scatter plot is shown in Fig. 5.9

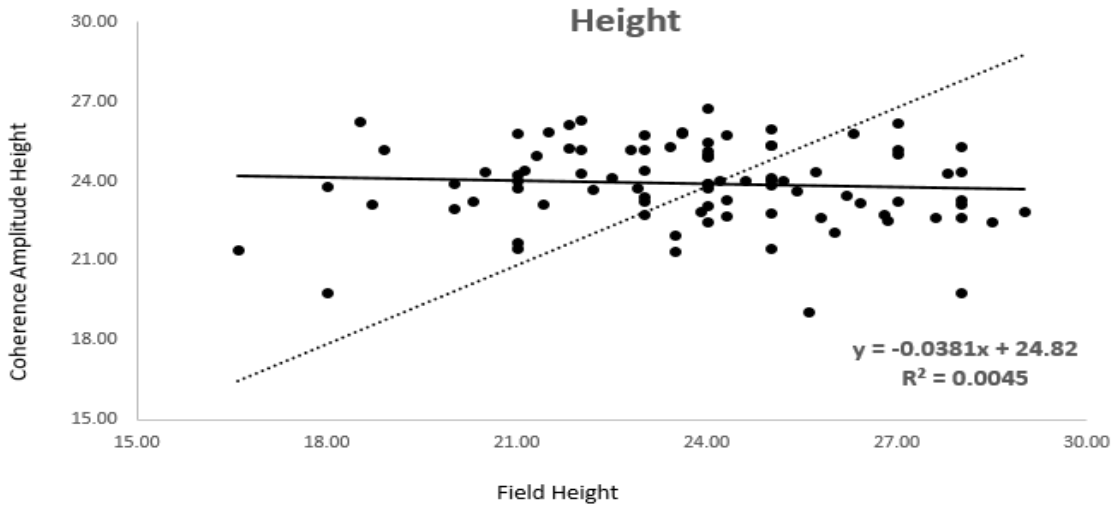


Figure 5.9 Scatter Plot between the Field height and CAI height before POA compensation for 2013

## 5.9 Forest height maps for dataset 2013 after POA compensation

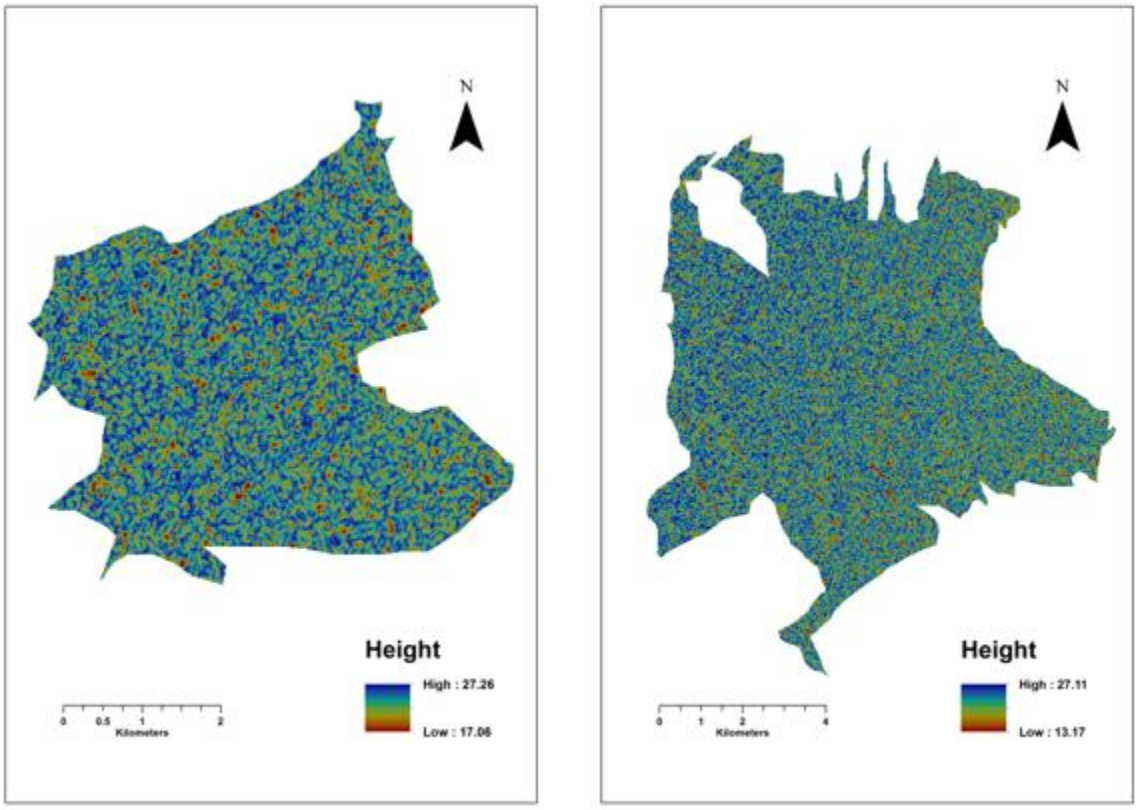


Figure 5.10 Tree height map of Thano range (left) and Barkot range (right) after POA compensation for 2013

## 5.10 Validation and accuracy assessment for dataset 2013 after POA compensation

Table 5.2 Table shows the data statistics for 2013 after POA compensation

| Forest Height Using | Sample Plot | Mean Height | Min Height | Max Height | Significance (p-value) |
|---|---|---|---|---|---|
| Field Data | 90 | 23.79 | 16.60 | 29 | 0.18 |
| Coherence Amplitude Inversion | 90 | 24.10 | 19.93 | 26.79 | 0.14 |

The average accuracy obtained after POA compensation is 88.49% with RMSE 3.25 m.

The table showing the p-value for both Field Height and CAI height is shown below: The p-value for CAI is greater than 0.05; it means that the CAI height plots are a part of the normally distributed population.

The scatter plot shows the comparison of field data with the measured data is shown in Fig. 5.11

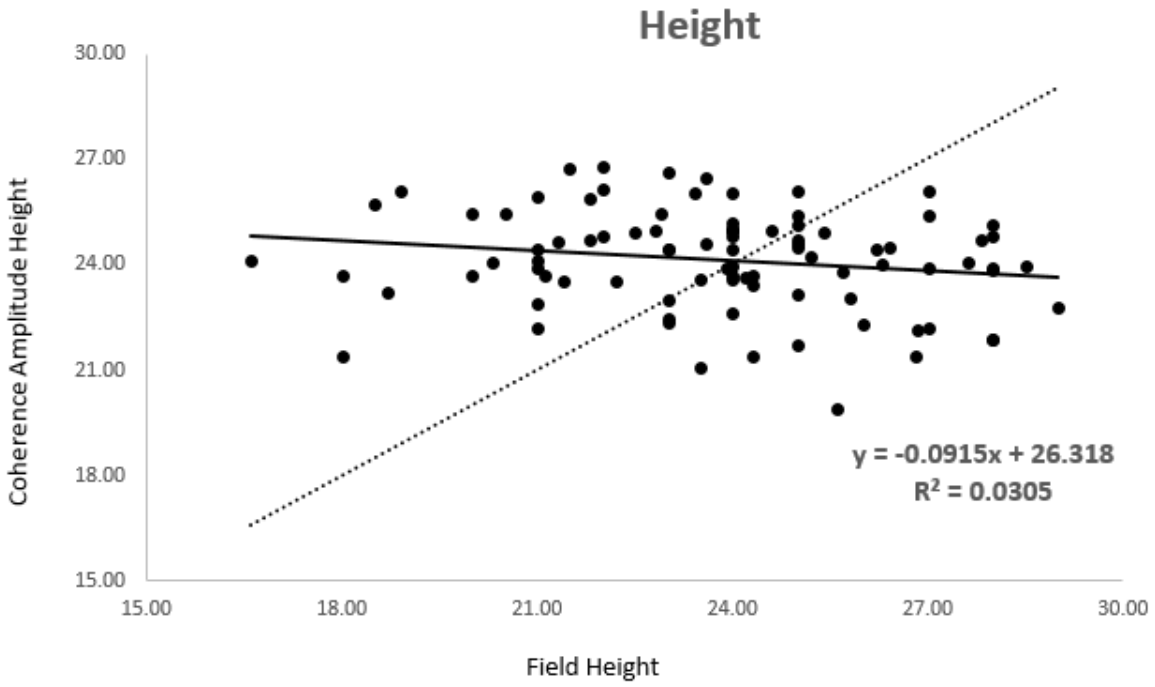


Figure 5.11 Scatter Plot between the Field height and CAI height after POA compensation for 2013

The graph showing the variation in tree height before and after POA compensation is shown in Fig. 5.12

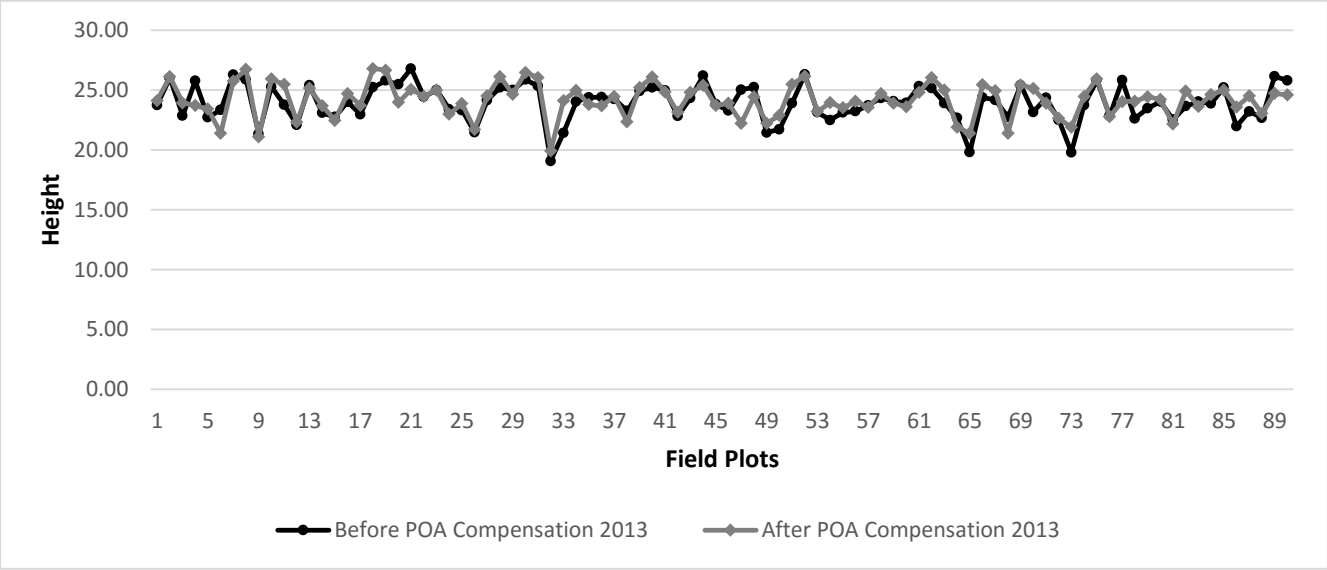


Figure 5.12 Variation in tree height before and after POA compensation for 2013

## 5.11 Forest height maps for dataset 2014 before POA compensation

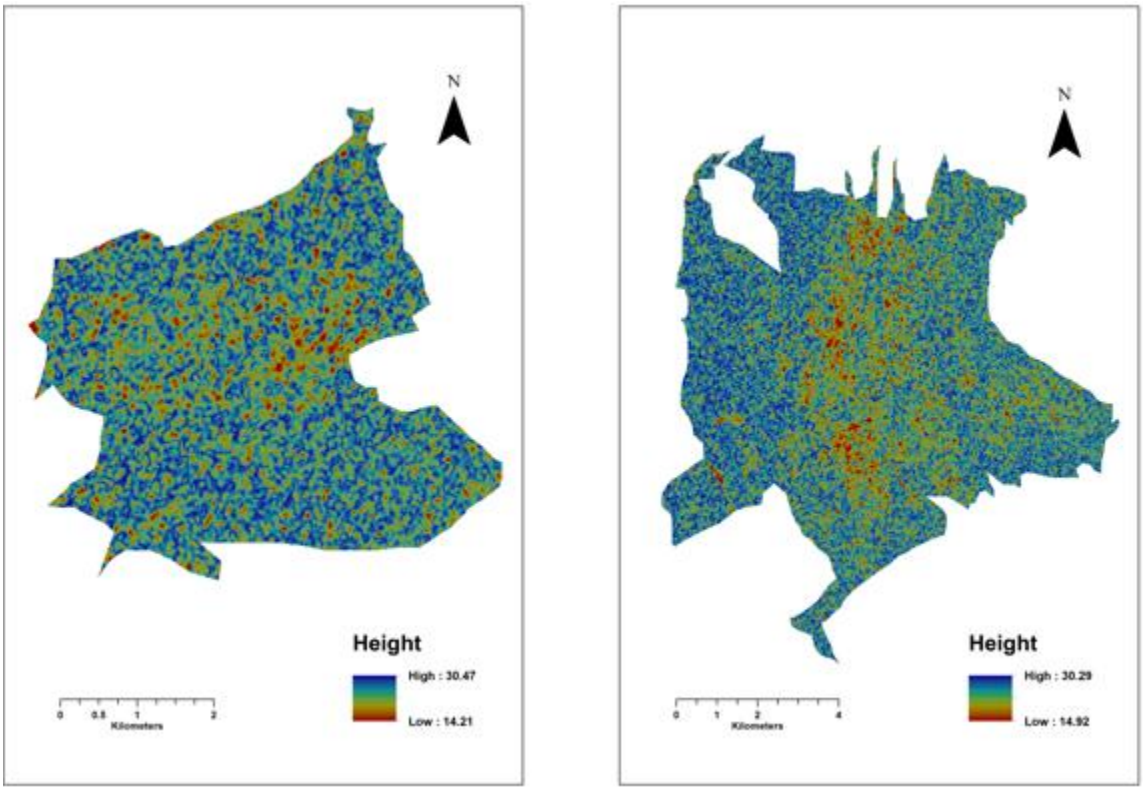


Figure 5.13 Tree height map of Thano range (left) and Barkot range (right) before POA compensation for 2014

## 5.12 Validation and accuracy assessment for dataset 2014 before POA compensation

Table 5.3 Table shows the data statistics for 2014 before POA compensation

| Forest Height Using | Sample Plot | Mean Height | Min Height | Max Height | Significance (p-value) |
|---|---|---|---|---|---|
| Field Data | 90 | 23.79 | 16.60 | 29 | 0.18 |
| Coherence Amplitude Inversion | 90 | 25.96 | 21.82 | 29.27 | 0.11 |

The average accuracy obtained after POA compensation is 85.59 with RMSE of 5 m.

The p-value for CAI is greater than 0.05; it means that the CAI height plots are a part of the normally distributed population.

The scatter plot showing the comparison of field data with the measured data is shown in Fig. 5.14

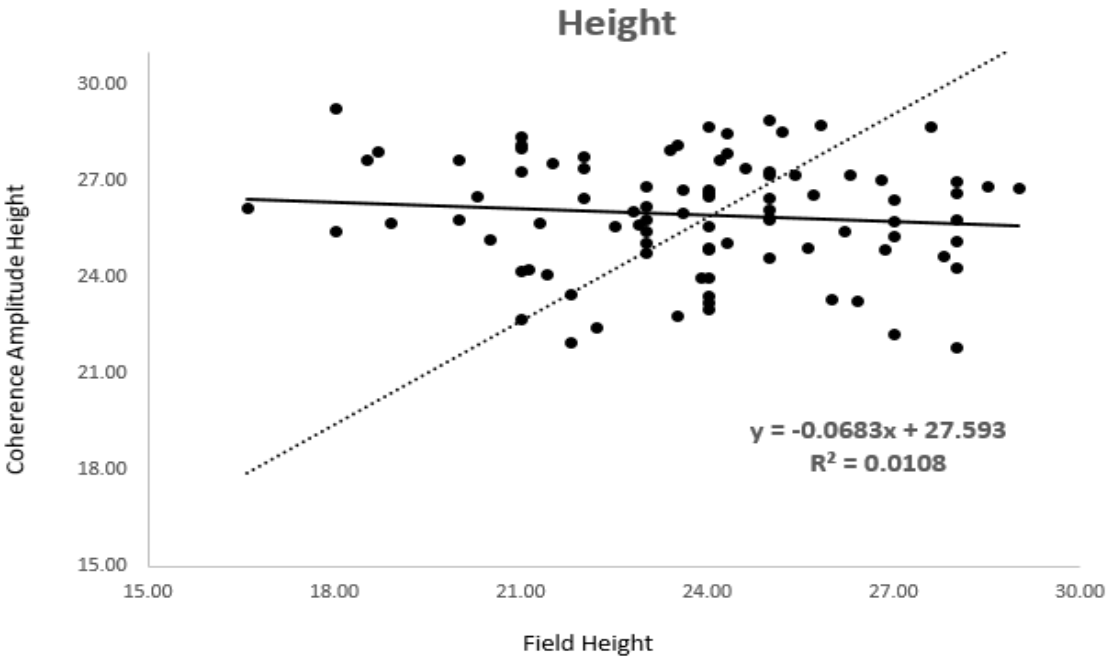


Figure 5.14 Scatter Plot between the Field height and CAI height before POA compensation for 2014

## 5.13 Forest height maps for dataset 2014 after POA compensation

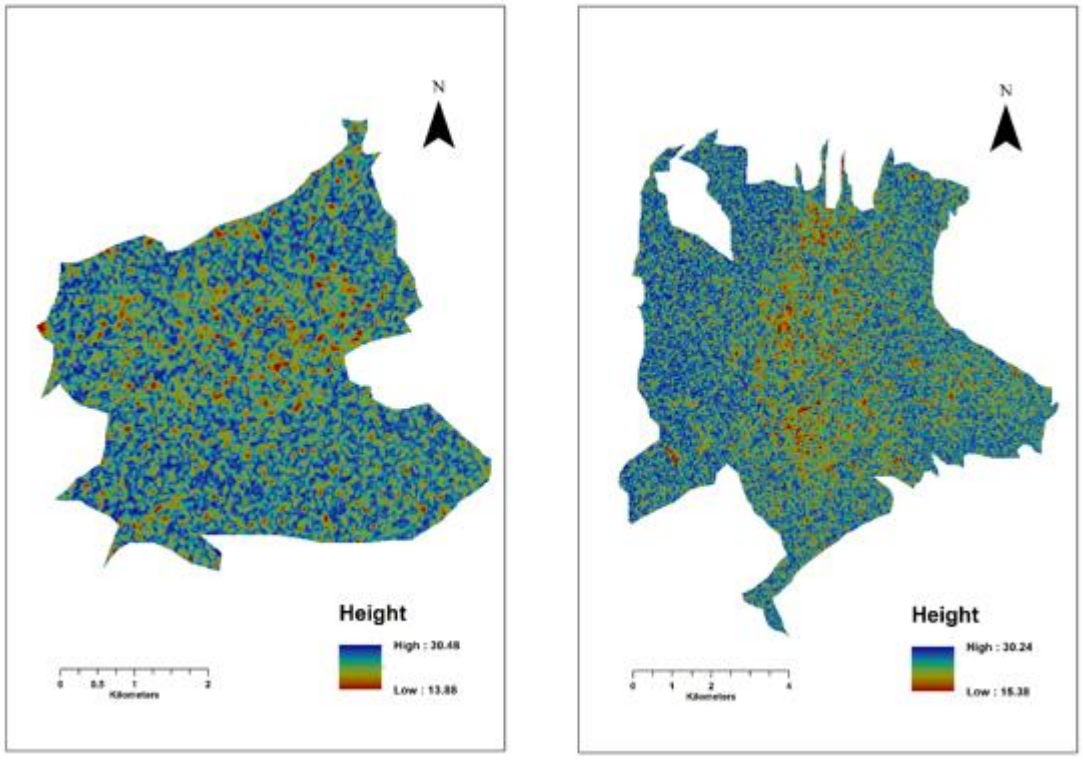


Figure 5.15 Tree height map of Thano range (left) and Barkot range (right) after POA compensation for 2014

## 5.14 Validation and accuracy assessment for dataset 2014 after POA compensation

Table 5.4 Table shows the data statistics for 2014 after POA compensation

| Forest Height Using | Sample Plot | Mean Height | Min Height | Max Height | Significance (p-value) |
|---|---|---|---|---|---|
| Field Data | 90 | 23.79 | 16.60 | 29 | 0.189 |
| Coherence Amplitude Inversion | 90 | 26.48 | 22.43 | 29.42 | 0.26 |

The average accuracy obtained after POA compensation is 84.32% with RMSE 4.25 m.

The p-value for CAI is greater than 0.05; it means that the CAI height plots are a part of the normally distributed population.

The scatter plot shows the comparison of field data with the measured data is shown in Fig. 5.16

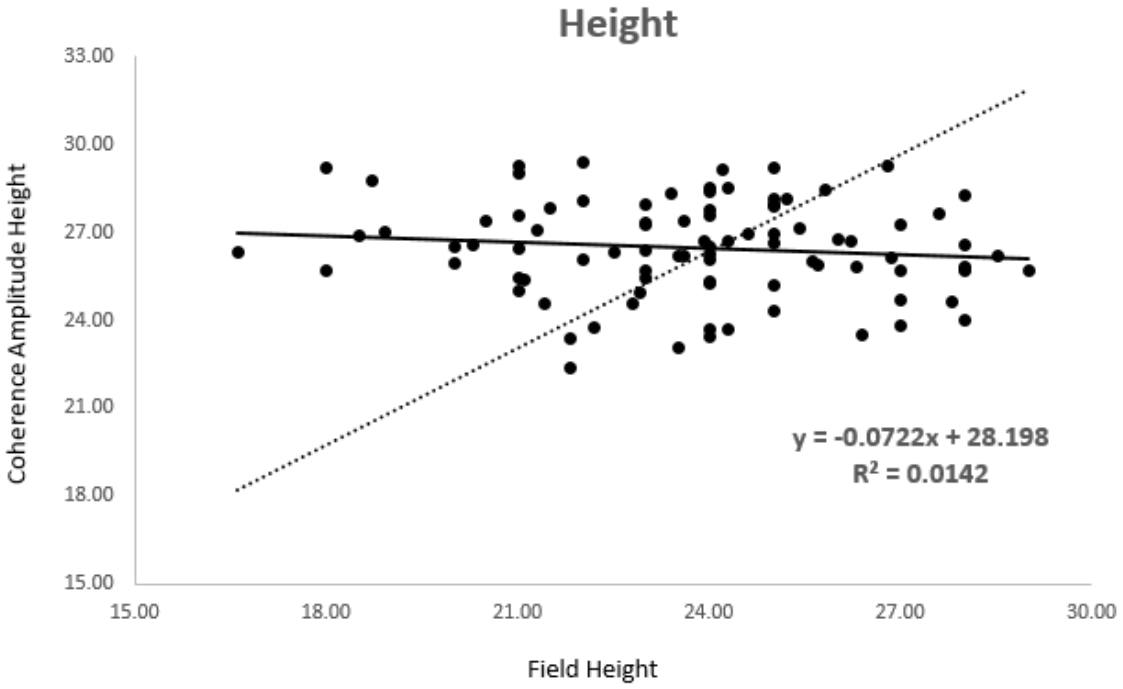


Figure 5.16 Scatter Plot between the Field height and CAI height after POA Compensation for 2014

The graph showing the variation in tree height before and after POA compensation is shown in Fig. 5.17

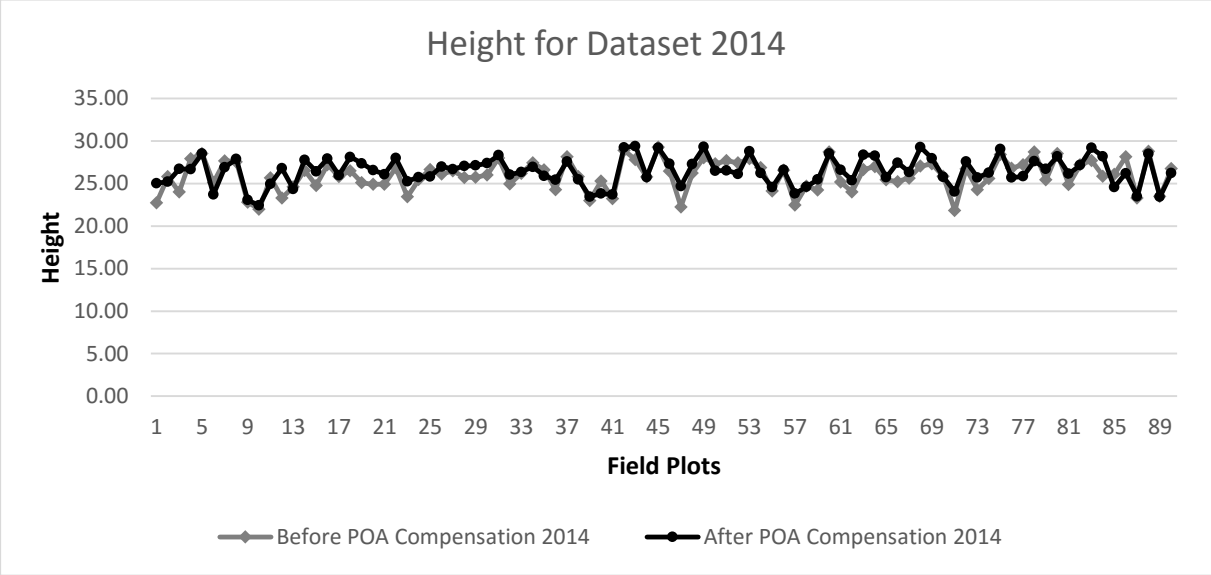


Figure 5.17 Variation in tree height before and after POA compensation for 2014

## 5.15 Discussion

The coherence analysis has been done by comparing the volume and double bounce scattering after POA compensation. Fig 5.1 and Fig 5.2 show the color composite image of 2013 before and after POA compensation. As observed from the image no changes were found but the Fig. 5.4 shows the comparison of the volume scattering present in the forest area. This graph did not show any trend for volume scattering. It may be because the POA compensation doesn't have much effect on the coherency matrix [$T_6$]. The statistics for the height measurement is shown in Table 5.1 and Table 5.2 for 2013 dataset. The mean height is the average height of all the 90 plots. The mean height after POA compensation has no change in the minimum and maximum height, but changes were observed between field height measurement and CAI measurement due to the error in estimation by measuring technique. The average accuracy after POA compensation is also almost similar. It means that if the average of volume scattering before and after POA compensation is taken then in both the cases result will be same with minor changes. It is also verified by the scatter plot in Fig 5.9 and Fig 5.11 which show similar trends with low R-square values. Fig 5.12 shows the variation in height which is almost similar. Table 5.1 shows that the measured height has some skewness and table 5.2 shows that the measured height is normally distributed. The color composite image of 2014 dataset is shown in Fig 5.3. A similar pattern was observed in the case of scattering as it was observed for 2013 dataset. Fig 5.6 indicates that the there is no pattern in volume scattering and Fig 5.7 indicates that double bounce scattering decreases after POA compensation. For the

tree height measurement in table 5.3 and 5.4, a slight change has been observed in minimum, maximum and average tree height resulting in a small decrease in average accuracy after POA compensation. Table 5.3 and 5.4 displays that measured height follows normal distribution curve. The fig 5.1 and fig 5.3 shows the change in coherence. This change in coherence is due to the change in incidence angle from higher to lower. Here this change from higher to lower in incidence angle results in high coherence in 2014 image. The increase in coherence has shown its effect on tree height measurement, table 5.1 and table 5.3 demonstrate the overestimation of tree height for 2014 dataset. The average accuracy is decreased from 88.88 % to 85.59 % due to the increase in residual values. The residual values are the difference between the field data and measured data. The decrease in average accuracy is also verified by the rmse error. The rmse error increased from 3.17 m for 2013 dataset to 5 m for 2014 dataset. Fig 5.9 and fig 5.14 shows the scatter plots for 2013 and 2014 dataset. The overestimation of height in 2014 dataset gives almost similar scatter plot as observed in 2013 dataset. It indicates that the pattern followed by field height and CAI measured height in 2014 is same as the pattern followed in 2013 by the field height and CAI measured height. The area comes under protected forest and no change was detected in this area. It was found that some plots have errors in height estimation. The source of error could be due to the difference in age of trees. It might also be possible that overestimation and underestimation in height within a dataset was due to the mixed species of trees and the closeness of measured height to the field height was due to the presence of homogeneous tree species. R square values for both the dataset was near to zero it indicates that the measured height does not fit the data at all. The possible reasons behind this was that the difference between the field height and measured height was large. The height measured with CAI amplitude technique have 88.88 % accuracy for 2013 dataset and 85.49 % accuracy for 2014 dataset. The height measure by technique seems reasonable but overestimation of height in dry river bed regions needsto be counter.

# 6. Conclusion

The main objective of the present study is to retrieve the tree height using PolInSAR based inversion modeling and show the effect on coherence after Polarization Orientation Angle compensation. The $T_6$ matrix was affected when POA shift compensation was applied on the scattering matrix. This results in the change of coherence observed and derived forest tree height. RADARSAT-2 uses C-band that interacts with the top of the canopy and cannot penetrate deeper in the case of dense forest areas. In SAR imaging, the wavelength of the microwave is considered as the reference length scale for the surface roughness. If the microwave length is greater than the surface fluctuation then the surface is considered as smooth and appear dark. Similarly if the surface fluctuation is greater than the microwave length then the surface would appear bright. The interaction with the top of the canopy gives unstable scatters results in low coherence values of 2013 dataset, but the images of 2014 dataset shows improvement in the coherence. It was found that the incidence angle of 2014 dataset is smaller than the incidence angle of 2013. Lower incidence angle can see through canopy gaps. It may be possible that the wave can interact with branches giving permanent scatter due to decrease in size of microwave length (C-band) as compared to the surface fluctuations. The image of 2013 has high incidence angle that interacts with the top of the canopy. The unstable scatters from the top of the canopy gives low coherence and appears dark. The average tree height was overestimated by 8 % in 2014 as compared to the height measure in 2013 because of high coherence that was the result of lower incidence angle. The changes in volume scattering and double bounce scattering of the individual dataset was observed due to the POA compensation. Fig 5.4 and Fig 5.6 of both datasets shows that there was no pattern found for the volume scattering after POA compensation but in Fig 5.5 and Fig 5.7, it was found that double bounce scattering decreases after POA compensation. So, it can be said that HVpVH coherence has random change in values but HHmVV coherence decreases after POA compensation. Thus it is concluded that no significant effect was observed after POA compensation on PolInSAR data. Tree height was measured using Coherence Amplitude Inversion based modeling technique. Based on table 5.1 and table 5.2 the average height was increased from 23.70 m to 23.91 m and 24.10 m. For table 5.3 and table 5.4, the average height was increased from 23.79 m to 25.90 m and 26.48 m. This average height increment was observed for 90 plots. Similarly, the average accuracy after POA compensation was decreased from 88.88 % to 88.49 % for 2013 dataset and from 85.49 % to 84.32 % for 2014 dataset. Thus, it is concluded that no POA shift compensation is required for PolInSAR based tree height estimation.

## 6.1 Recommendations:

Recommendations have been listed to enhance the reliability of the present study.

- Coherence and backscatter technique will be implemented to improve the overestimated height obtained in dry river bed regions.
- Larger incidence angle provides better result, so dataset with multi-frequency and multi-incidence angle may be tested to find out the suitability of incidence angle for tree height estimation.
- Non-availability of LIDAR for tree height validation is the main limitation. With more pair of PolInSAR data, the validation of present study would be more accurate.
- Barkot and Thano range have almost flat topography. The impact of slope on POA can be studied for PolInSAR data on the different study area.
- The heterogeneous species of trees in a forest should be studied using present methodology.
- Different bands of the spectrum with high penetration capability should be used to access the reliability of the present study.
- Comparison of different techniques for tree height estimation can also be studied using present methodology.

# 7. List of References:

Ahmed, O. S., Franklin, S. E., Wulder, M. a., & White, J. C. (2015). Characterizing stand-level forest canopy cover and height using Landsat time series, samples of airborne LiDAR, and the Random Forest algorithm. *ISPRS Journal of Photogrammetry and Remote Sensing*, *101*, 89–101. http://doi.org/10.1016/j.isprsjprs.2014.11.007

Balmer, R., & Hartl, P. (2000). Synthetic aperture radar interferometry. *Proceedings of the IEEE*, *88*(3), 1–54. http://doi.org/10.1109/5.838084

Balzter, H., Rowland, C. S., & Saich, P. (2007). Forest canopy height and carbon estimation at Monks Wood National Nature Reserve, UK, using dual-wavelength SAR interferometry. *Remote Sensing of Environment*, *108*(3), 224–239. http://doi.org/10.1016/j.rse.2006.11.014

Boerner, W.-M., Moreira, a., Papathanassiou, K. P., Hajnsek, I., Pottier, E., Ferro-Famil, L., … Lukowski, T. (2003). Need for developing multi-band single and multiple pass POLinSAR monitoring platforms in air and space. *IGARSS 2003. 2003 IEEE International Geoscience and Remote Sensing Symposium. Proceedings (IEEE Cat. No.03CH37477)*, *1*(C), 7929–7931. http://doi.org/10.1109/IGARSS.2003.1293796

Caicoya, A. T., Kugler, F., Hajnsek, I., & Papathanassiou, K. P. (2015). Vertical forest structure characterization for the estimation of above ground biomass.

Champion, H. G., & Seth, S. K. (2005). *A Revised Survey Of The Forest Types Of India*. Retrieved from http://www.indianbooks.co.in/bookmart/revised-survey-of-the-forest-types-of-india.html

Chandola, S. (2014). Polarimetric SAR Interferometry for Forest Aboveground Biomass Estimation, (March). Retrieved from http://www.itc.nl/library/papers_2014/msc/gfm/chandola.pdf

Chehade, B. E. H., & Ferro-Famil, L. (2013). Polarimetric tomography for forest parameters retrieval. *International Geoscience and Remote Sensing Symposium (IGARSS)*, *1*(4), 4340–4343. http://doi.org/10.1109/IGARSS.2013.6723795

Chen, X., Wang, C., & Zhang, H. (2007). Robust forest height extraction using polarimetric SAR interferometry. *Geoscience and Remote Sensing …*, (40501044), 1603–1606. Retrieved from http://ieeexplore.ieee.org/xpls/abs_all.jsp?arnumber=4423119

Cloude, S., & Corr, D. (2003). Tree-height Retrieval Using Single Baseline Polarimetric Interferometry. *Proceedings of the Workshop on POLinSAR - Applications of SAR Polarimetry and Polarimetric Interferometry (ESA SP-529)*, (1), 10. Retrieved from http://adsabs.harvard.edu/full/2003ESASP.529E..28C

Cloude, S. R. (2005). *POL-InSAR TRAINING COURSE*.

Cloude, S. R. (2010). *Polarisation applications in remote sensing*.

Cloude, S. R., Brolly, M., & Woodhouse, I. H. (2009). A study of forest vertical structure estimation using coherence tomography coupled to a macro-ecological scattering model. *Geoscience and Remote Sensing*

*Symposium,2009 IEEE International,IGARSS 2009*, *4*(1), 717–720. http://doi.org/10.1109/IGARSS.2009.5417477

Cloude, S. R., & Papathanassiou, K. P. (1998). Polarimetric SAR Interferometry, *36*(5), 1551–1565.

Cloude, S. R., & Papathanassiou, K. P. (2003). Three-stage inversion process for polarimetric SAR interferometry. *IEE Proceedings - Radar, Sonar and Navigation*, *150*(3), 125. http://doi.org/10.1049/ip-rsn:20030449

Cloude, S. R., & Papathanassiou, K. P. (2008). Forest vertical structure estimation using coherence tomography, (1), 275–278.

Cloude, S. R., & Pottier, E. (1996). A review of target decomposition theorems in radar polarimetry. *IEEE Transactions on Geoscience and Remote Sensing*, *34*(2), 498–518. http://doi.org/10.1109/36.485127

European Space Agency. (2016).

Feldpausch, T. R., Lloyd, J., Lewis, S. L., Brienen, R. J. W., Gloor, M., Monteagudo Mendoza, a., … Phillips, O. L. (2012). Tree height integrated into pantropical forest biomass estimates. *Biogeosciences*, *9*(8), 3381–3403. http://doi.org/10.5194/bg-9-3381-2012

Freeman, A., & Durden, S. L. (1998). A three-component scattering model for polarimetric SAR data. *IEEE Transactions on Geoscience and Remote Sensing*, *36*(3), 963–973. http://doi.org/10.1109/36.673687

Garestier, F., Dubois-Fernandez, P. C., & Papathanassiou, K. P. (2008). Pine forest height inversion using single-pass X-band PolInSAR data. *IEEE Transactions on Geoscience and Remote Sensing*, *46*(1), 59–68. http://doi.org/10.1109/TGRS.2007.907602

Gatelli, F., Monti Guamieri, a., Parizzi, F., Pasquali, P., Prati, C., & Rocca, F. (1994). The wavenumber shift in SAR interferometry. *IEEE Transactions on Geoscience and Remote Sensing*, *32*(4), 855–865. http://doi.org/10.1109/36.298013

Goward, S. N., & Williams, D. L. (1997). Landsat and Earth Systems Science : Development of terrestrial monitoring. *Photogrammetric Engineering and Remote Sensing*, *63*(July), 887–900. Retrieved from http://cat.inist.fr/?aModele=afficheN&cpsidt=2825225

Gwenzi, D., & Lefsky, M. A. (2014). Modeling canopy height in a savanna ecosystem using spaceborne lidar waveforms. *Remote Sensing of Environment*, *154*, 338–344. http://doi.org/10.1016/j.rse.2013.11.024

Hagberg, J. O., Ulander, L. M. H., & Askne, J. (1995). Repeat-pass SAR Interferometry Over Forested Terrain. *IEEE Transactions on Geoscience and Remote Sensing*, *33*(2), 331–340. http://doi.org/10.1109/36.377933

Hongjun, C., Bin, Z., & Maoliu, L. (2007). Parameter inversion models based on PolInSAR images. *2007 1st Asian and Pacific Conference on Synthetic Aperture Radar Proceedings, APSAR 2007*, (92), 751–754. http://doi.org/10.1109/APSAR.2007.4418720

Hunter, M. O., Keller, M., Victoria, D., & Morton, D. C. (2013). Tree height and tropical forest biomass estimation. *Biogeosciences*, *10*(12), 8385–8399. http://doi.org/10.5194/bg-10-8385-2013

Husch, B., W Beers, T., & A. Kershaw, J. (2002). *Wiley: Forest Mensuration, 4th Edition - Bertram Husch, Thomas W. Beers, John A. Kershaw* (4th ed.). Retrieved from http://as.wiley.com/WileyCDA/WileyTitle/productCd-0471018503.html

Institute of Electronics and Telecommunications of Rennes -University of Rennes. (2016). ESAPolSARpro.

Iribe, K., & Sato, M. (2007). Analysis of polarization orientation angle shifts by artificial structures. *IEEE Transactions on Geoscience and Remote Sensing*, *45*(11), 3417–3425. http://doi.org/10.1109/TGRS.2007.905973

Jin, Y.-Q., & Xu, F. (2013). *Wiley: Polarimetric Scattering and SAR Information*. Retrieved from http://as.wiley.com/WileyCDA/WileyTitle/productCd-1118188136.html

Krieger, G., Cloude, S. R., & Papathanassiou, K. P. (2005). Spaceborne Polarimetric SAR Interferometry : Performance Analysis and Mission Concepts, 3272–3292.

Krieger, G., Moreira, A., Fiedler, H., Hajnsek, I., Werner, M., Younis, M., & Zink, M. (2007). TanDEM-X : A Satellite Formation for. *IEEE Transactions on Geoscience and Remote Sensing*, *45*(11), 3317–3341. http://doi.org/10.1109/TGRS.2007.900693

Kugler, F., Lee, S. K., Hajnsek, I., & Papathanassiou, K. P. (2015). Forest Height Estimation by Means of Pol-InSAR Data Inversion: The Role of the Vertical Wavenumber. *IEEE Transactions on Geoscience and Remote Sensing*, *53*(10), 5294–5311. http://doi.org/10.1109/TGRS.2015.2420996

Lavalle, M., Pottier, E., Solimini, D., Desnos, Y. L., Miranda, N., Rosich, B., & Santuari, M. (2009). A new approach for polinsar forest parameters inversion: RESULTS USING THE ESA ALOS-PALSAR PROTOTYPE PROCESSOR. *European Space Agency, (Special Publication) ESA SP*, *668 SP*(April), 3–6.

Lee, J., & Ainsworth, T. L. (2011). the Effect of Orientation Angle Compensation on Polarimetric, *49*(1), 849–852.

Lee, J. S., Schuler, D. L., & Ainsworth, T. L. (2000). Polarimetric SAR data compensation for terrain azimuth slope variation. *IEEE Transactions on Geoscience and Remote Sensing*, *38*(5 I), 2153–2163. http://doi.org/10.1109/36.868874

Lee, J.-S., & Pottier, E. (2009). Polarimetric radar imaging: from basics to applications, 440. Retrieved from http://books.google.com/books?hl=en&lr=&id=1nAvp2HW_gwC&oi=fnd&pg=PR19&dq=Polarimetric+Radar+Imaging,+From+basics+to+applications&ots=v1-XVB2v9e&sig=R5LdBVofXDDJ-cgkEJsD37MGaTs\nhttp://books.google.co.in/books?id=1nAvp2HW_gwC

Lee, J. Sen, Schuler, D. L., Ainsworth, T. L., Krogager, E., Kasilingam, D., & Boerner, W. M. (2002). On the estimation of radar polarization orientation shifts induced by terrain slopes. *IEEE Transactions on Geoscience and Remote Sensing*, *40*(1), 30–41. http://doi.org/10.1109/36.981347

Li, F. K., & Goldstein, R. M. (1990). Studies of multibaseline spaceborne interferometric synthetic aperture radars. *IEEE Transactions on Geoscience and Remote Sensing*, *28*(1), 88–97. http://doi.org/10.1109/36.45749

Li, Z., Guo, M., Wang, Z., & Zhao, L. (2014). Forest-height inversion using repeat-pass spaceborne polInSAR data. *Science China Earth Sciences*, *57*(6), 1314–1324. http://doi.org/10.1007/s11430-013-4669-3

Lulu, T., & Ruliang, Y. (2008). Investigation on tree height retrieval with polarimetric sar interferometry. *International Geoscience and Remote Sensing Symposium (IGARSS)*, *5*(1), 546–549. http://doi.org/10.1109/IGARSS.2008.4780150

Massonnet, D., & Claude-Jean, S. (2008). *Imaging with Synthetic Aperture Radar*. Retrieved from https://www.crcpress.com/Imaging-with-Synthetic-Aperture-Radar/Massonnet-Souyris/9780849382390

Mette, T., Papathanassiou, K., Hajnsek, I., Pretzsch, H., & Biber, P. (2004). Applying a common allometric equation to convert forest height from Pol-InSAR data to forest biomass. *IGARSS 2004. 2004 IEEE International Geoscience and Remote Sensing Symposium*, *1*(C), 269–272. http://doi.org/10.1109/IGARSS.2004.1369013

Mette, T., Papathanassiou, K. P., Hajnsek, I., & Zimmermann, R. (2002). Forest Biomass Estimation using Polarimetric SAR Interferometry. *Proceedings of the IEEE International Geoscience and Remote Sensing Symposium (IGARSS)*, *2*(0), 817–819.

Minh, N. P., & Zou, B. (2013). A Novel Algorithm for Forest Height Estimation from PolInSAR Image. *International Journal of Signal Processing, Image Processing and Pattern Recoginition*, *6*(2), 15–32.

Moreira, A., Prats-iraola, P., Younis, M., Krieger, G., Hajnsek, I., & Papathanassiou, K. P. (2013). A Tutorial on Synthetic Aperture Radar. *IEEE Geoscience and Remote Sensing Magazine*, (march).

Neumann, M., Ferro-famil, L., & Reigber, A. (2010). Estimation of Forest Structure , Ground , and Canopy Layer Characteristics From Multibaseline Polarimetric Interferometric SAR Data, *48*(3), 1086–1104.

Nilsson, M. (1996). Estimation of tree heights and stand volume using an airborne lidar system. *Remote Sensing of Environment*, *56*(95), 1–7. http://doi.org/10.1016/0034-4257(95)00224-3

Papathanassiou, K., & Cloude, S. R. (2016). *SINGLE vs MULTI-POLARIZATION INTERFEROMETRY*.

Paris, C., & Bruzzone, L. (2015). A Three-Dimensional Model-Based Approach to the Estimation of the Tree Top Height by Fusing Low-Density LiDAR Data and Very High Resolution Optical Images, *53*(1), 467–480.

Percy, K. E., Jandl, R., Hall, J. P., & Lavigne, M. (2005). The Role of Forests in Carbon Cycles , Sequestration and Storage. *Economic Analysis*, (3), 5.

Pottier, E., & Lee, J.-S. (2009). *Polarimetric Radar Imaging*. CRC Press.

Praks, J., Hallikainen, M., Seppanen, J., & Hyyppa, J. (2009). BOREAL FOREST HEIGHT ESTIMATION WITH SAR INTERFEROMETRY AND LASER MEASUREMENTS. *IGARSS*, (July 2005), 308–311.

Prati, C., Rocca, F., Guarnieri, A. M., & Damonti, E. (1990). Seismicmigration for sar focussing: interferometrical applications, *28*, 627–640.

Prati, C., Rocca, F., Guarnieri, A. M., & Pasquali, P. (1994). *Report on ERS-1 SAR Interferometric Techniques and Applications*.

RCoreTeam. (2015). R: A Language and Environment for Statistical Computing.

Reigber, A., & Moreira, A. (2000). First demonstration of airborne SAR tomography using multibaseline L-band data. *IEEE Transactions on Geoscience and Remote Sensing*, *38*(5 I), 2142–2152. http://doi.org/10.1109/36.868873

Sefercik, U. G., & Dana, I. (2008). Crucial Points of Interferometric Processing for Dem Generation Using High Resolution Sar Data.

Singh, S. P. (2010). *Impact of Forest Degradation on Carbon Density in Soil and Vegetation of*. *International Journal of Climatology*.

Solberg, S., Næsset, E., Gobakken, T., & Bollandsås, O.-M. (2014). Forest biomass change estimated from height change in interferometric SAR height models. *Carbon Balance and Management*, *9*(1), 5. http://doi.org/10.1186/s13021-014-0005-2

Solberg, S., Weydahl, D. J., & Næsset, E. (2003). SAR forest canopy penetration depth as an indicator for forest health monitoring based on leaf area index ( LAI ), 2–6.

Steinbrecher, U., Zink, M., Moreira, A., Bachmann, M., Böer, J., Schulze, D., & Krieger, G. (2013). Tandem-X Mission : Overview , Status and Outlook. *ISPRS Hannover Workshop 2013*, *XL*(May), 21–24.

Suárez, J. C., Ontiveros, C., Smith, S., & Snape, S. (2005). Use of airborne LiDAR and aerial photography in the estimation of individual tree heights in forestry. *Computers and Geosciences*, *31*(2), 253–262. http://doi.org/10.1016/j.cageo.2004.09.015

Subudhi, S. P., & Shah, R. K. (2009). *WORKING PLAN OF DEHRADUN FOREST DIVISION*.

Tan, L., Yang, R., & Yu, W. (2009). Accuracy improvement of maximum likelihood inversion of forest height with polinsar. *International Geoscience and Remote Sensing Symposium (IGARSS)*, *3*, 654–657. http://doi.org/10.1109/IGARSS.2009.5417845

Tebaldini, S. (2009). Algebraic synthesis of forest scenarios from multibaseline PolInSAR data. *IEEE Transactions on Geoscience and Remote Sensing*, *47*(12), 4132–4142. http://doi.org/10.1109/TGRS.2009.2023785

Touzi, R., Boerner, W. M., Lee, J. S., & Lueneburg, E. (2004). A review of polarimetry in the context of synthetic aperture radar: Concepts and information extraction. *Canadian Journal of Remote Sensing*, *30*(3), 380–407. http://doi.org/10.5589/m04-013

Touzi, R., Lopes, A., Bruniquel, J., & Vachon, P. W. (1999). Coherence estimation for SAR imagery. *IEEE Transactions on Geoscience and Remote Sensing*, *37*(1 PART 1), 135–149. http://doi.org/10.1109/36.739146

Turner, D. P., Cohen, W. B., Kennedy, R. E., Fassnacht, K. S., & Briggs, J. M. (1999). Relationships between leaf area index and Landsat TM spectral vegetation indices across three temperate zone sites. *Remote Sensing of Environment*, *70*(1), 52–68. http://doi.org/10.1016/S0034-4257(99)00057-7

Wang, W. (2006). Optimal baseline design and error compensation for bistatic spaceborne InSAR. *European Space Agency, (Special Publication) ESA SP*, *2005*(610).

Wang, Y. W. Y., Hess, L. L., Filoso, S., & Melack, J. M. (1994). Canopy penetration studies: modeled radar backscatter from Amazon floodplain forests at C-, L-, and P-band. *Proceedings of IGARSS '94 - 1994 IEEE International Geoscience and Remote Sensing Symposium*, *2*, 1060–1062. http://doi.org/10.1109/IGARSS.1994.399343

Waring, R. H., Way, J. B., Hunt, E. R., Morrissey, L., Ranson, K. J., Weishampel, J. F., … Franklin, S. E. (1995). Imaging radar for ecosystem studies. *BioScience*. http://doi.org/10.2307/1312677

Wegmüller, U., & Werner, C. L. (1995). SAR interferometric signatures of forest. *IEEE Transactions on Geoscience and Remote Sensing*, *33*(5), 1153–1161. http://doi.org/10.1109/36.469479

Woodhouse, I. H. (2005). *Introduction to Microwave Remote Sensing* (Vol. 2). CRC Press. Retrieved from https://books.google.com/books?id=CtNPyoLxEPMC&pgis=1

Xie, Q., Zhu, J., Wang, C., & Fu, H. (2014). Boreal Forest Height Inversion Using E-SAR PolInSAR Data Based Coherence Optimization Methods and Three-Stage Algorithm 2014 Third International Workshop on Earth Observation and Remote Sensing Applications, 0–4.

Yamada, H., Yamaguchi, Y., Rodriguez, E., Kim, Y., & Boerner, W. M. (2001). Polarimetric SAR interferometry for forest canopy analysis by using the super-resolution method. *IGARSS 2001. Scanning the Present and Resolving the Future. Proceedings. IEEE 2001 International Geoscience and Remote Sensing Symposium (Cat. No.01CH37217)*, *3*(C), 7031–7033. http://doi.org/10.1109/IGARSS.2001.976759

Yamaguchi, Y., Moriyama, T., Ishido, M., & Yamada, H. (2005). Four-component scattering model for polarimetric SAR image decomposition. *IEEE Transactions on Geoscience and Remote Sensing*, *43*(8), 1699–1706. http://doi.org/10.1109/TGRS.2005.852084

Zebker, H. A., & Goldstein, R. M. (1986). Topographic mapping from interferometric synthetic aperture radar observations. *Journal of Geophysical Research*, *91*(B5), 4993. http://doi.org/10.1029/JB091iB05p04993